This is a preprint, the final version is subject to change, of the American Mineralogist (MSA)
Cite as Authors (Year) Title. American Mineralogist, in press.
DOI: https://doi.org/10.2138/am-2019-6764

revision 1

Nanoscale study of lamellar exsolutions in clinopyroxene from olivine gabbro: recording crystallization sequences in iron-rich layered intrusions

Wenyuan Gao[1,2], Cristiana L. Ciobanu[2], Nigel J. Cook[2], Ashley Slattery[3], Fei Huang[1,*], Daoheng Wang[1]

[1]*Key Laboratory of Ministry of Education on Safe Mining of Deep Metal Mines, and School of Resources and Civil Engineering, Northeastern University, Shenyang 110819, China*

[2]*School of Chemical Engineering, The University of Adelaide, SA 5005, Australia*

[3]*Adelaide Microscopy, The University of Adelaide, SA 5005, Australia*

ABSTRACT

Pyroxene exsolutions and associated Fe–Ti-oxides and spinels are described in a sample of olivine gabbro representing the Middle Zone of the Panzhihua layered intrusion, Southwest China, part of the Emeishan LIP. High-angle annular dark-field scanning transmission electron microscope imaging, electron diffraction and energy dispersive spectroscopy reveal complex multi-stage exsolution relationships in the host clinopyroxene. The studied assemblage is common in gabbroic rocks and comprises: subcalcic diopside and lamellar clinoenstatite (<1 wt% Ca). Two sets of exsolved clinopyroxene lamellae are observed. Only one is, however, well-developed as lamellae oriented approximately parallel to (801) of diopside, making an angle of ~10 to 11° with the (100) planes, or the *c* axis, of both phases. These are the so-called "100" lamellae with a perfect fit along *a*-crystallographic axes when viewed down to [010] zone axis. Crosscutting exsolutions of Fe–(Ti)-oxides are relatively common throughout the same host clinopyroxene. Apart from ilmenite and magnetite with variable Ti-content, hercynite is a minor yet ubiquitous phase. The nanoscale study indicates a sequence of fine-scale processes: from higher-*T* (~1030–1100 °C): (I) (clino)enstatite

* Corresponding author. E-mail address: huangfei@mail.neu.edu.cn

exsolutions in low-Ca diopside; followed by (II) slightly Ca-richer diopside overgrowths and high-*T* titanomagnetite exsolution in diopside; to lower-*T* (<450 °C) (III) titanomagnetite exsolutions into ulvöspinel+magnetite; followed by (IV) sub-solidus re-equilibration in clinopyroxenes and among Fe–Ti oxides + hercynite. Using exact phase boundary theory, pressures of lamellar exsolution within the host diopside are estimated as ~2 GPa with an error of ± ≤1 GPa. The present study of complex exsolutions in clinopyroxene demonstrates that a nanoscale approach can help constrain *P–T–X* evolution during formation of layered intrusions.

Keywords: High-angle annular dark field scanning transmission electron microscopy; Clinopyroxene; Titanomagnetite; Liquid-magmatic ore deposits; Sequence of exsolution.

INTRODUCTION

Natural clinopyroxenes of intermediate composition within the $CaMgSi_2O_6$ – $CaFeSi_2O_6$ – $Mg_2Si_2O_6$ – $Fe_2Si_2O_6$ quadrilateral are frequently observed to exsolve into lamellae of Ca-rich and Ca-poor composition, i.e., pigeonite in augite or diopside (Fig. 1a, b) (Buseck et al. 1980). The exsolution structure of pyroxene is not only found in terrestrial rocks (Moore et al. 2001), but also lunar and meteorite samples (Ferraris et al. 2003). Analysis of pyroxene exsolution enables cooling rates and geological evolution to be constrained (McCallister 1978).

Augite with pigeonite exsolutions and *vice-versa* are known from layered intrusions: e.g., Duluth Gabbro and Stillwater Complexes, USA; Bushveld Complex, South Africa; Skaergaard Intrusion, Greenland (Robinson et al. 1971; 1977 and references therein; Nakajima and Hafner 1980; Kitamura et al. 1981). Relative lattice orientations between two exsolved phases can be used for application of the theory of optimal phase boundaries (Bollman 1970; Robinson et al. 1971; 1977) and subsequent calculation of exsolution temperatures (Robinson et al. 1977) and pressures based upon them (Liu et al. 2007; Zhao et al. 2017).

Lattice orientation can be obtained by single-crystal X-ray diffraction, transmission electron microscopy (TEM) and electron backscatter diffraction (EBSD). Terminology to describe exsolution

lamellae of 'monoclinic pyroxenes in monoclinic pyroxene hosts' has varied in the literature. Robinson et al. (1971) introduced the term "(100)" to describe lamellae that would be rational with a perfect fit along the *c*-crystallographic axes, and "(001)" to describe lamellae that would be rational with a perfect fit along the *a*-crystallographic axes, when viewed down to the [010] zone axis. The petrogenetic value of such exsolutions as "fossil indicators of lattice parameters at high *T* and pressure" is discussed using specimens from the Bushveld Main Zone Gabbro (Robinson et al. 1977), in which multiple sets of lamellae were used for measurement of lattice parameters at different temperatures, with ensuing suggestions for development of geothermometers. Independent of the phase boundary theory, a graphical two-pyroxene thermometer was designed from experimentally-determined Ca–Mg–Fe pyroxene phase relations at 800–1200 °C and <1 atmosphere up to 15 kbar, combined with calculated phase equilibria for the diopside–enstatite and hedenbergite–ferrosilite joins (Lindsley 1983). The miscibility gap between the diopside and enstatite widens and its consulate point expands to higher-*T* with increasing pressure (Lindsley 1980). Such behavior was confirmed and refined by thermodynamic modelling results that were consistent with all experimental data available at the time for the enstatite–diopside join (Gasparik, 1990).

Although exsolutions of orthoenstatite from diopside are common in peridotites from both ophiolites and mantle xenoliths, exsolution of "clinoenstatite in diopside" is reported and considered a good petrogenetic indicator for metamorphic ultra-high pressure (UHP) rocks (Bozhilov et al. 1999; Liu et al. 2007). Compositionally comparable pyroxene pairs are nonetheless known from layered intrusions such as the Bushveld Complex, i.e., low-Ca 'pigeonite I' ($Wo_2En_{56}Fs_{42}$) exsolved as (001) lamellae from Ca-rich augite ($Wo_{44}En_{38}Fs_{18}$) giving calculated *T* at ~1000–1050 °C, the highest among all observed exsolutions sets (Fig. 1a, b) (Robinson et al. 1977).

Many experimental studies were devoted to pyroxenes with low Ca contents such as those from the enstatite–ferrosilite and pigeonite solid solution series [$(Mg,Fe,Ca)^{M2}(Mg,Fe)^{M1}Si_2O_6$] because they display complex polymorphism and phase transition with pressure and temperature (e.g., Brown et al. 1972; Angel et al. 1992; Hugh-Jones et al. 1994; Christy and Angel 1995; Arlt et al. 1998; 2000;

Tribaudino et al. 2000, 2002, 2003; Cámara et al. 2002; Alvaro et al. 2011). At atmospheric conditions, most of these pyroxenes have primitive space groups, monoclinic $P2_1/c$ or orthorhombic *Pbca*, and crystal structures comprising two differently oriented $[Si_2O_6]$-chains. The phase transitions involving orthopyroxenes are reversible, whereas both high temperature (*HT*) and high pressure (*HP*) phase transitions in clinopyroxenes are displacive and involve symmetry increase to space group $C2/c$ as the $[Si_2O_6]$ chains change their geometry and alignment with one another (Arlt et al. 2000, and references therein; Cámara et al. 2002; Alvaro et al. 2011). Such data are important for mapping *P–T–X* phase stability and indicate that the temperature of the transformation decreases linearly with M_2 cation size, from ~1200 °C in end-member enstatite to ~150 °C for Ca-, Fe-, Mn-substituted pyroxenes (Arlt et al. 2000, and references therein). In the same study, the positive correlation between *P* and *T* during the transition was defined as ~149 °C/GPa based on *in-situ P–T* experiments (synchrotron powder diffraction study in a heated diamond-anvil cell) on kanoite (ideally $MnMgSi_2O_6$). It was found that increasing pressure also changes the displacive transition from first order to continuous. Using data from Arlt et al. (2000), formation of pigeonite ($En_{47}Fs_{43}Wo_{10}$; Fig. 1b) lamellae in space group $C2/c$ was estimated at pressures up to 2 GPa after which $P2_1/c$ transition took place at ~1100 °C with a minimum at 850 °C in mantle-related xenocrysts within alkaline basalt from Hannuoba, Hebei Province, China (Brizi et al. 2003).

Two TEM studies of pyroxene exolutions, in the Alpe Arami garnet lherzolite, Swiss Alps (Bozhilov et al. 1999), and in garnet peridotite from the Dabie Mountains UHP metamorphic terrane, China (Liu et al. 2007) documented (100) lamellae of clinoenstite in diopside and augite with comparable boundary angles at ~22° and 18°, respectively. In both studies, the authors concluded that the measured $P2_1/c$ low-clinoenstatite results from an initial *HP* $C2/c$ monoclinic polymorph of clinoenstatite and invoke nm-scale antiphase domains in their argument in support for such interpretation. Exsolutions are considered to occur at comparable conditions, i.e., >250 km (~8 GPa) at upper mantle temperature in the Alpe Arami (Bozhilov et al. 1999) and at ~300 km (~9 GPa) in the Dabie Mountain (Liu et al. 2007). The latter study presents a calculation routine for estimating

exsolution pressures using the exact phase boundary theory and goes on to suggest pressures as high as 12 GPa for the Alpe Arami "clinoenstatite". Arlt et al. (2000) however contest the characterisation of the Alpe Arami "clinoenstatite" as a pigeonite ($En_{80}Fs_{13}Wo_7$; Fig. 1b) and point out that the temperature estimate ignores the effects of M2 site cations (Fe and Ca) substitution on the stability of *C*2/*c* polymorphs. Arlt et al. (2000) revise conditions for the Alpe Arami occurrence to ~850 °C and lower depth (~220 km or ~7.8 GPa).

Mantle lherzolite xenoliths within Cenozoic basalts from the Mingxi area, Fujian Province, China were analyzed by Zhao et al. (2017) using EBSD to measure the boundary angle at ~22° between the *c* axes of (100) orthopyroxene (enstatite–pigeonite) lamellae and host diopside. Based on the exact phase boundary theory and using data from Tribaudino et al. (2000) for clinopyroxene at high *P*, the authors developed a new protocol, distinct from that of Liu et al. (2007), to estimate exsolution pressure at ~4 GPa. Zhao et al. (2017) only considered the effect of pressure and ignored the influence of temperature because the mantle lherzolite xenoliths crystallized under high pressure conditions. It was suggested that the exsolution lamellae probably formed during decompression associated with transport from upper mantle to surface.

Pyroxenes from mafic plutonic and metamorphic rocks also commonly contain oriented, thin lamellae of Fe–Ti-oxides (Fleet et al. 1980; Doukhan et al. 1990). Such inclusions are important in paleomagnetic and rock magnetic studies for their varied magnetizations (Renne et al. 2002). Feinberg et al. (2004) determined the lattice orientations of magnetite exsolutions using EBSD. On this basis, they used optimal phase boundary theory to determine the temperature at which magnetite exsolved to be 840 ± 50 °C.

Ramdohr (1969) illustrated extensive examples of Fe–Ti-oxides and their characteristic textures. Numerous studies have since addressed relationships among Fe–Ti-oxides within the $FeO–TiO_2–Fe_2O_3$ compositional triangle (Bowles et al. 2011, and references therein). Phases observed as intergrowths in Fe–Ti-oxides belong to tie-lines between (i) magnetite and ulvöspinel, and (ii) ilmenite and hematite/maghemite, defining the titanomagnetite and hemoilmenite solid solution

series with cubic and rhombohedral lattices, respectively. The subsolidus phase diagram for the titanomagnetite solid solution series was re-assessed as symmetric with a consolute temperature of <455 ºC based upon calculations on the suppression of coherent spinodal textures (Price 1981).

Crystallographically-oriented intergrowths between spinels and ilmenite ('trellis' textures), which are often interpreted as a subsolidus re-equilibration based upon an experimentally deduced oxidation-exsolution model (Buddington and Lindsley 1964). Such a model is, however, considered inadequate to explain the complexity of intergrowths between magnetite, ilmenite and ulvöspinel in natural rocks (e.g., Mücke 2003). Alternative, late-stage subsolidus reduction and O_2-conserving reaction schemes were proposed (e.g., Haggerty 1972; Haselton and Nash 1975). All such models are very popular for interpretation of cooling histories among Fe–Ti-oxides with implications for ore-forming processes, particularly in mafic intrusions.

Microintergrowths of ulvöspinel and ilmenite obtained experimentally at 1300 ° C and at low fO_2 (Lattard 1995) show exsolution caused by vacancy relaxation in the spinel according to the substitution: $Fe_2^{2+} \leftrightarrow Ti^{4+} + \square$; and no indication of redox processes. Such models, applicable to lunar basalts, back-up O_2-conserving conditions rather than redox processes. Krasnova and Krezer (1995), in their experimental study on the nature of fine and ultrafine lamellae in titanomagnetite also question the general validity of the 'oxidation-exsolution' model of Buddington and Lindsley (1964). Based on the excess of FeO instead of Fe_2O_3, as well as the occurrence of 2–3 additional diffraction lines on the X-ray powder patterns of titanomagnetite with ilmenite exsolutions, they suggest such exsolutions are likely due to simple electron exchange without changing the number of cations.

Petrogenetic models can be better constrained if the complexity of exsolutions in both pyroxene pairs or among Fe–Ti oxides is addressed at appropriate scales of observation, from micron- to nanoscale. Here we study such exsolutions identified at the micron-scale as pairs of (clino)pyroxene exsolutions crosscut by Fe–Ti-oxides exsolutions within olivine gabbro from the Panzhihua intrusion, SW China (Gao et al. 2017). To do so, we undertake a nanoscale study focused on identification of the minerals in these exsolutions and their fine intergrowths. We apply the optimal phase boundary

153 theory of Robinson et al. (1977) using the approach proposed by Zhao et al. (2017) to estimate the
154 exsolution pressure of pyroxenes. Results represent valuable evidence supporting evolutionary
155 models for magmatic systems and for processes involved in forming layered intrusions.

156 ## BACKGROUND

157 The Panzhihua intrusion is a layered gabbroic intrusion in the central part of the Emeishan Large
158 Igneous Province (ELIP), Southwest China (Zhou et al. 2005). Like other similar intrusions in the
159 province, Panzhihua contains significant ore deposits of Fe, Ti and V (Song et al. 2013). Inferred
160 crystallization pressure is ~3–5 kbar from mineral composition and geological relationships (Pang et
161 al. 2015) although Shellnutt and Jahn (2010) considered that the Panzhihua intrusion could have
162 crystallized at or below ~1.5 kbar. This discrepancy can be explained in terms of intrusion
163 crystallization at ~3–5 kbar (corresponding to a depth of ~9–15 km) and formation of a residual silicic
164 magma, which migrated upwards and crystallized in a chamber at the base of the flood basalt pile
165 (Pang et al. 2015). Crystallization temperature was ~1200 °C estimated on the basis of anhydrous
166 mineral composition and comparison to high-Ti basalts of the ELIP (Pang et al. 2015). In an earlier
167 study, however, Pang et al. (2008) contend that abundant crystallization of Fe–Ti oxides at an early
168 stage from a magma enriched in Fe and Ti but low in SiO_2 implies fractionation of mantle-derived
169 melts at higher pressures (~10 kbar). Still higher pressures/depths are envisioned in the latest models
170 for ELIP magmatism considering a magma plumbing system centered on a mantle plume (Tao et al.
171 2015). In this reconstruction, the ELIP is rooted onto primitive picrite magma at the lower
172 crust/lithospheric boundary (~55 km depth; ~20 kbar) and contains two other reservoirs: a high-Mg
173 basaltic magma in the middle crust at <33 km (~10 kbar); and an upper basaltic magma chamber in
174 the upper crust <16 km (~5 kbar) (Tao et al. 2015).

175 The occurrence of reversals in the patterns of mineral and bulk-rock composition over the vertical
176 extent of the intrusion (Pang et al. 2009; Song et al. 2013) indicates that the Panzhihua intrusion
177 represents an open system magma chamber. There are, however, still diverse views on genetic models
178 for the Fe–Ti–V-oxide ores. Some workers propose that these formed via direct crystallization and

accumulation from an immiscible Fe–Ti–V-rich liquid (Zhou et al. 2005; Hou et al. 2012). Others have advocated fractional crystallization and gravitational accumulation of Fe–Ti–V-oxide to explain deposit formation (Pang et al. 2009; Pêcher et al. 2013; Song et al. 2013). At Panzhihua, magnetite–ilmenite cooling paths on fO_2-T diagrams are invoked among the lines of evidence to support a model of titanomagnetite crystal-accumulation instead of ore formation via magma immiscibility (Pang et al. 2008). In contrast, Tan et al. (2016) suggest that some ilmenite lamellae exsolved directly from a cation-deficient solid solution invoking the same isochemical substitution suggested by Lattard (1995).

Recently, in-depth petrographic study (Gao et al. 2017) has also shown evidence of a more complex history of melt emplacement and an overprint in which K-bearing minerals (micas and K-feldspar) have replaced pre-existing minerals in the gabbro. Gao et al. (2017) attribute this metasomatism to fluids derived from felsic intrusions that are present within the area. In another ELIP intrusion (Hongge), Xing and Wang (2017) proposed a late-stage fluid-induced hydrothermal metasomatism to explain wide variation in REE-signatures in fluorapatite.

Clinopyroxene is one of the main minerals throughout the intrusion with compositions across the boundary between diopside and augite (Gao et al. 2017). The Fe–(Ti)-oxide exsolutions are relatively common throughout the clinopyroxene but the pyroxene exsolutions identified by Gao et al. (2017) are limited to smaller domains within host clinopyroxene. Considering the petrogenetic value of such exsolution pairs and the complexity of titanomagnetite (Fe–Ti-oxides) throughout the ores it is critical to verify the speciation and relationships between such minerals hosted by clinopyroxene.

ANALYTICAL METHODOLOGY

All analytical work was performed on one-inch polished blocks using instruments housed at Adelaide Microscopy, The University of Adelaide. A FEI Quanta 450 scanning electron microscope (SEM) with energy-dispersive X-ray spectrometry (EDS) and back-scatter electron (BSE) imaging capabilities was used at an accelerating voltage of 20 kV and beam current of 10 nA.

Cross-section imaging and transmission electron microscope (TEM) sample preparation was performed on a FEI Helios Nanolab 600 DualBeam™ Focused Ion Beam Scanning Electron Microscope (FIB-SEM). Procedures outlined by Ciobanu et al. (2011) were followed in extraction and thinning of TEM foils by ion beam (Ga^{+}) milling.

Selected area electron diffraction (SAED) and High-Resolution (HR)-TEM imaging in Bright Field (BF) mode were obtained using a Philips CM200 TEM equipped with a LaB_6 source, double-tilt holder and Gatan digital camera, operated at 200 kV. The illumination area for electron diffractions is 200 nm. Measurements on the diffractions and image analysis were performed using DigitalMicrograph™ 1.83.842. Electron diffractions were indexed using WinWulff™ 1.5.2 and data from the American Mineralogist Crystal Structure Database (http://rruff.geo.arizona.edu/AMS/amcsd.php).

High-angle annular dark field scanning transmission electron microscopy (HAADF-STEM) imaging and EDS measurements were performed on an ultra-high resolution, probe-corrected, FEI Titan Themis S/TEM operated at 200 kV, with ~5 nm EDS spot size. This was equipped with X-FEG electron source, aberration correction, Fischione HAADF detector and Super-X EDS geometry. Probe correction delivered sub-Ångstrom-scale spatial resolution and an inner collection angle greater than 50 mrad were used for HAADF. The Super-X detector provides geometrically symmetric EDS detection with an effective solid angle of 0.8 sr. The image analysis and Fast Fourier Transform (FFT) were processed by TEM Imaging & Analysis 4.15.

We measured the orientation of exsolution lamellae relative to the host pyroxene directly on TEM images (both BF and HAADF STEM). We estimated the pyroxene exsolution pressure using the approach in Zhao et al. (2017) as follows. The average, minimum and maximum angles obtained from measurements were used for calculating the fit for lattice vectors as expressed in the exact phase boundary theory of Robinson et al. (1977) with lattice parameters interpolated from Tribaudino et al. (2000) within an iteration sequence across a range of pressures. The fit is considered for the pressure value that shows minimal difference between the lattice vectors of two phases.

This is a preprint, the final version is subject to change, of the American Mineralogist (MSA)
Cite as Authors (Year) Title. American Mineralogist, in press.
DOI: https://doi.org/10.2138/am-2019-6764

SAMPLES

The study was carried out on pyroxene from an olivine gabbro representing the Middle Zone of the Panzhihua intrusion (sample PL52F in Gao et al. 2017). Estimated modal mineralogy is 50% plagioclase, 35% clinopyroxene, 4% olivine, 10%, Fe–Ti-oxides and 1% sulfides. This sample shows a marked deformation of the silicate assemblages, in which Fe–Ti-oxides are redistributed across the layering and within small shears. One clinopyroxene grain with lamellar exsolutions of both Fe–Ti-oxides and pyroxene was selected for preparation of two TEM foils by FIB-SEM (Fig. 1c, d). As compositional data for individual lamellae could not be obtained by microprobe analysis, Gao et al. (2017) assessed compositional variation across a profile crosscutting the lamellae (Fig. 1c). Data from Gao et al. (2017) show a subcalcic diopside (average: $Wo_{43.5}En_{42.9}Fs_{13.6}$; Table 1) and give a spread of points extending along a line vertically downwards, roughly 5% of the way into the augite field (Fig. 1b). This average is probably very close to the host composition since the volume occupied by lamellae within each analytical point can be considered small (Fig. 1c). Two FIB-prepared TEM foils were cut from the same host grain with the purpose to better characterize the exsolutions, both pyroxenes and Fe–Ti oxides.

Foil 1 was cut across an area containing only pyroxene lamellae and Foil 2 was cut across both types of lamellar exsolutions. This grain also contains fine (~50 μm-sized) grains of amphibole and olivine. Low-resolution and HAADF-STEM and Bright Field (BF) TEM imaging shows details of the lamellae throughout the two foils (Fig. 2). In contrast to dense, parallel sets of pyroxene lamellae throughout the two foils, there is only a single titanomagnetite lamella, ~2 μm wide and ~10 μm in length (Fig. 2b, d). The pyroxene lamellae display variable widths (~70 nm) and lengths (~2 to ~16 μm) (Fig. 2a–d). A second set of short, pyroxene lamellae is identified in Foil 2 with orientation at ~106° to the main lamellae set (Fig. 2e).

RESULTS

The two foils were studied using BF TEM imaging and electron diffractions prior to HAADF-STEM imaging and STEM EDS mapping. EDS spectra, with 5 nm spot size, were collected from thin areas representative of minerals in the associations.

Pyroxene pairs

Electron diffractions obtained from pyroxenes in both foils indicate the two pyroxenes form epitaxial intergrowths along the a^* axis and are both monoclinic (Fig. 3a–c). As the electron beam is moved across a given lamella when the specimen is tilted down to [010] and [011] zone axes in host Ca-clinopyroxene (augite or diopside), the SAED patterns show satellite reflections along a^* (Fig. 3b, c). Spinodal exsolution, as documented by, for example, Brizi et al. (2003), is inferred from the sinusoidal distribution of such satellite reflections on SAEDs down to the [010] and [011] zone axis (Fig. 3b, c). In contrast, the host and lamellar pyroxene are undistinguishable on other zone axes, e.g., $[1\bar{1}1]$ (Fig. 3d). In this case the SAEDs could not be indexed using $C2/c$ or $P2_1/c$ space groups for the host: monoclinic calcic pyroxene (diopside or augite) (Cameron et al. 1973; Clark et al. 1969), or for the exsolved clinopyroxene: pigeonite or clinoenstatite (Morimoto and Güven 1970; Tribaudino et al. 2002), respectively. The measured distances at ~5 Å are attributable to $h0l$, with h, $l \neq 2n$ reflections for both phases are incompatible with symmetry in $C2/c$ and $P2_1/c$ space groups (Fig. 3d). This SAED can be indexed instead as zone axis $[1\bar{1}1]$ for both diopside and clinoenstatite using the space groups $P2_1/n$ (14) and $P2/n$ (13), respectively. Reflection conditions for $P2_1/n$ are: $h0l$, $h+l=2n$; $h00$, $h=2n$; $0k0$, $k=2n$; $00l$, $l=2n$ and for $P2/n$ are: $h0l$, $h+l=2n$; $0k0$, $k=2n$; $00l$, $l=2n$. This solution is concordant with the measured ~79º angle between the $(\bar{1}01)^*$ and $(110)^*$ lattice vectors on $[1\bar{1}1]$ zone axis (Fig. 3d).

HAADF-STEM imaging was undertaken on both foils by tilting the specimen on [010] zone axis in host pyroxene (Fig. 4a, b). The compositions of host and lamella clinopyroxene were measured by EDS (spot size 5 nm) on one of thinnest areas at the top of Foil 1 (Figs. 2a and 4a). Results confirm that the host is a Ca-bearing species whereas the pyroxene in the lamellae is Mg-higher and lacks

measurable Ca (Fig. 4c, d). Both pyroxenes contain Fe, whereby the lamellae are richer than the host. This can explain the brighter shade on HAADF-STEM images (Figs. 4a and 5a).

Although the EDS spectrum in Figure 4d shows no measurable Ca (<1 wt% CaO, below the detection limit of the EDS detector) this can nonetheless be considered as a nominal small value (~0.8–0.9 CaO; ~1 mol% Wo). The composition of the lamella in Wo–En–Fs space can thus be estimated as $Wo_1En_{62}Fs_{37}$ (Table 1; Fig. 1b, hereafter called clinoenstatite, Cen) by extending the projection of data points from subcalcic diopside to low-Ca clinopyroxene.

Bright Field TEM and HAADF-STEM imaging show coherent boundaries between the two clinopyroxenes (Fig. 5a and Fig. S1 in Supplemental Material). In detail, such boundaries show stepwise rather than parallel alignment between rows of bright atoms (Fig. 4a). No antiphase domains were identified in the lamellae. The arrangements of bright atoms on HAADF-STEM images also display alternating distances of 500 and 520 pm along the *a* axis defining *a*=9.8 Å corresponding to clinoenstatite, whereas in diopside the arrays of bright atoms show equal spacings at *a*=4.7 Å (Fig. 5a). The narrower spacings between the bright atoms are also slightly darker on HAADF-STEM images (Fig. 5b). The bright atoms are attributable to cation (Mg, Fe and Ca) distribution in the two pyroxenes by comparison with crystal structure simulations down to the *b* axis (Fig. 5c).

Direct measurement on HAADF STEM and BF TEM images (Fig. 5a; Fig. S1 in Supplemental Material) of angles between the host–lamella boundary and the *c* axis of each phase gives values in the range θ = 10 to 11° (mean of 12 measurements 10.68±0.36°; Table 2). The orientation of the diopside plane relative to the Cen lamella is obtained by the intercept between the a^* axis rotated at angle θ with $(h02)^*$ lattice vector, in our case at (801) for rotation θ = ~11° (Fig. 4b). The relationships between (801) of diopside, making an angle of ~10 to 11° with the (100) planes or the *c* axis of both phases are also shown on Fig. 2c.

Textures and mineral associations within titanomagnetite

HAADF-STEM imaging of the titanomagnetite lamella in Foil 2 indicates more complex mineral intergrowths than previously recognized (Fig. 6). Imaging was done with the specimen tilted on the

[$\bar{1}$10] zone axis of magnetite. Relationships between the titanomagnetite lamella and host pyroxene show crosscutting relationships despite minor displacement of clinoenstatite (Fig. 6a).

To better understand the speciation, textures and phase relationships in the assemblage, imaging and STEM EDS mapping were undertaken at the top (thinner area; Fig. 6b, c), and in the middle-lower part of the titanomagnetite lamella (Figs. 6e and 7; Fig. S2 in Supplemental Material). Trails 1 are wider, several hundred nm in width, and have a patchy appearance with variable contrast on the HAADF-STEM images. In contrast, Trails 2 are only a few nm in width and show a two-phase assemblage comprising ilmenite as small, stubby grains (tens to hundreds of nm in size) growing perpendicular to thin arrays of Al-rich spinel (Fig. 6e, f). A substructure, changing orientation across the crosscutting clinopyroxene lamella, is observed along Trails 1 from the middle-lower part of the titanomagnetite (Fig. 6d). The same ilmenite + spinel assemblage is identified at junctions between the two trail types (Fig. 6f). In this case the spinel occurs as coarser lamellae (up to 10 nm wide) rather than along the trails. High-resolution images show atom arrays within titanomagnetite and ilmenite with parallel orientation to one another (Fig. 6g, h). The two trail sets contain the same Al-rich spinel (hercynite) + ilmenite assemblage identified from EDS spectra obtained from the thinner areas (Fig. 6i). It is noted that magnetite with little Ti is present along Trails 2.

STEM EDS mapping shows that the zebra-like pattern consists of alternating layers of magnetite and Ti–Al-bearing magnetite (Trails 1; Fig. 7). In detail, the wider (hundreds of nm) domains with Ti–Al-bearing magnetite show a finer, Ti-rich and Ti-poor lamellar sub-pattern. In addition, these domains are dotted by nanometer-scale grains of hercynite. The orientation of such lamellae changes from horizontal to vertical relative to the layering on either side of the crosscutting clinoenstatite lamella (Fig. S2 in Supplemental Material). Coarser spinel and ilmenite occur along Trails 2. Other trace elements present at measurable concentrations include V and Mn; both are enriched in ilmenite along Trails 2 (Fig. S2 in Supplemental Material).

SAEDs obtained from the magnetite within the lamella by tilting the specimen on several zone axes (Fig. 8) show satellite reflections with 3-fold periodicity on different lattice vectors (Fig. 8a, c–

e). Such satellite reflections are typically present when the electron diffraction is obtained from magnetite from areas along the trails. Distances of 4.2 Å measured on SAEDs of magnetite down to $[\bar{1}10]$ zone axis (Fig. 8b) from areas free of inclusions correspond to reflections *00l*, $l \neq 4n$, incompatible with $Fd3m$ symmetry. They can, however, be indexed instead using the $F\bar{4}3m$ space group (Fleet 1986). SAEDs on $[1\bar{1}2]$ zone axis in magnetite from areas with crosscutting trails show satellite reflections that can be indexed as ilmenite on [1100] zone axis if the space group $P63/m$ is used instead of $R\bar{3}$ (Fig. 8e, f). Measured distances between satellite reflections observed on SAEDs patterns from other zone axes in magnetite, e.g., [010], $[1\bar{2}1]$ or $[\bar{1}10]$, could not attributed to ilmenite.

High-resolution HAADF-STEM imaging of assemblages with the specimen tilted down to $[\bar{1}10]$ zone axis in magnetite (Fig. 9) shows relationships among the three minerals along the trails. Sharp boundaries and triple junctions between spinel and magnetite, or spinel, magnetite and ilmenite, respectively, are highlighted by atom arrays with parallel orientation to one another (Fig. 9a, b). In detail, however, boundaries between magnetite and ilmenite display stepwise atomic arrangements indicative of small-scale replacement or re-equilibration (Fig. 9c, d). Nonetheless the two minerals are crystallographically oriented to one another whereby the (111)* axis in magnetite is parallel with the *c** axis in ilmenite (Fig. 9d). Atomic arrangement in magnetite down to the $[\bar{1}10]$ zone axis shows atoms of higher and lower intensity (Fig. 9e). The observed pattern shows an atom arrangement comprising weaker intensity atoms as asymmetric rings around atoms of the highest intensity with a better fit to the crystal structure model using the $F\bar{4}3m$ (Fleet 1986) rather than the $Fd3m$ space group (Fig. 9f).

Overprint along boundaries between titanomagnetite and clinopyroxene

The boundaries between the titanomagnetite lamellae and pyroxene show, in places, areas with patchiness in terms of contrast on the HAADF-STEM images (Fig. 10a). In one area at the top of the lamella, amphibole can be inferred from EDS spectra. Imaging displays variable intergrowths

between brighter strips with wider and narrower spacing that are different from those recorded in the clinopyroxenes (Fig. 10b, c). Such atom arrays could not be imaged at higher resolution due to the variable thickness and relief along the titanomagnetite–pyroxene boundary. The presence of amphibole as narrow lamellae, hundreds of nm in length, is also identified close to where clinoenstatite crosscuts the titanomagnetite lamella (Fig. 10d). Sharp boundaries between magnetite and diopside are nonetheless present (Fig. 10e) and these differ from scalloped morphologies occurring at places where amphibole formation occurs (Fig. 10f).

DISCUSSION

Crystal structure modifications

In this study both pyroxenes and titanomagnetite display crystal structural modifications relative to commonly considered polymorphs or ideal spinel structures, respectively. Chisholm (1982) in a useful summary of published work (see references therein) discussed lowering of symmetry in clinopyroxenes using the 'I-beam' concept, defined as 'a strip of M cations sandwiched between two chains of SiO_4 tetrahedra' when using a general formula: $(M_2)(M_1)T_2O_6$, where M_2 = Na, Ca, Mg, Fe^{2+}, Li, and represents the cation in irregularly-coordinated sites linking adjacent I-beams; M_1 = Mg, Fe^{2+}, Al, Fe^{3+}, Mn, and represents the octahedrally-coordinated cation sandwiched between the tetrahedral chains; and T = Si, Al, the tetrahedrally-coordinated cation in the TO_4 chains. In such a model, the TO_4 tetrahedra can be rotated about a^* to fit the M-octahedral chains and still retain the *c*-glide symmetry of the pyroxenes (Chisholm 1982). However, lowering of $C2/c$ symmetry may occur due to subdivision of (M_1, M_2), and/or T sites because of cation ordering to achieve minimal energy in response to variable composition, or to strain introduced in the crystal-structure. The space groups $P2_1/n$ and $P2/n$ considered here for diopside and clinoenstatite, respectively, are among the four 2/*m* subgroups of the *C*2/c space group suggested (Chisholm 1982). Violation of *C* centering and *c* glide extinctions in space group $C2/c$ are known for pyroxenes of the omphacite group (e.g., $P2/n$; Curtis et al. 1975).

Magnetite ($Fe^{2+}Fe_2^{3+}O_4$) has an inverse spinel crystal structure with *Fd*3*m* space group in which the oxygen atoms form an approximatively cubic close-packed array with one Fe^{3+} per formula unit in a tetrahedral coordination (T sites) whereas the Fe^{2+} and remaining Fe^{3+} atoms are randomly distributed in octahedral positions (M sites) (e.g., Fleet 1981). The inverse spinel structure is related to the high-electric conductivity of magnetite interpreted either as 'electron hopping' (exchange of Fe^{2+} and Fe^{3+} in the M sites (Verwey and Boer 1936), or to a semi-conductor character associated with a defect structure of natural magnetite at room temperature (Fleet 1981). X-ray studies show that some magnetites have non-centrosymmetric $F\bar{4}3m$ structure (forbidden reflections; e.g., *00l* with $l \neq 4$) with distinct T1 and T2 sites (Fleet 1986), as also interpreted from SAEDs of magnetite in this study (e.g., Fig. 8b). Comparable SAEDs representing the $[1\bar{1}0]$ zone axis of magnetite with reflections violating *Fd*3*m* symmetry are shown in other TEM studies (e.g., Woensdregt et al. 1983; Wang et al. 1989); the latter authors nonetheless attribute such reflections to double diffraction. Taking into consideration the better fit between our HAADF-STEM images (Fig. 9f–h) and the model of Fleet (1986), we conclude that the $F\bar{4}3m$ structure is feasible for magnetite studied here.

Exsolution pressure of pyroxene lamellae determined by exact phase boundary theory

Based on the measurements in Table 2, we can assess the lamella within the observed space, the plane of the FIB cut (perpendicular to the polished block surface), being of "type (100)" according to the notation of Robinson et al. (1971, 1977), whereby the acute θ angle is measured relative to the c^* axis in each phase (Fig. 11a). We can use the equations derived for 'exact phase boundary theory for pyroxene exsolution' of Robinson et al. (1977) to obtain a geometric fit between lamellae and host pyroxene lattices that minimizes interface energy. This best fit varies as the lattice parameters of the lamellae and host change with temperature or/and pressure.

Consider the two monoclinic phases, which have identical *b*-dimensions and similar structure and are intergrown so that their [010] planes are parallel. An exact phase boundary between the two phases lies at a plane that is oriented parallel to the common *b*-direction and contains a vector **Y** directed

parallel to the common [010] plane. The magnitude of the unit-repeat of vector **Y** in terms of the phase 1 and phase 2 unit-cell parameters is given by Equations (1) and (2):

$$|\mathbf{Y_1}| = (a_1^2x_1^2 + c_1^2z_1^2 + |2a_1c_1\cos\beta_1\, x_1z_1|)^{1/2} \text{ for phase 1 (lamella)} \quad (1)$$

$$|\mathbf{Y_2}| = (a_2^2x_2^2 + c_2^2z_2^2 + |2a_2c_2\cos\beta_2\, x_2z_2|)^{1/2} \text{ for phase 2 (host)} \quad (2)$$

where *x* and *z* are coordinates of the vector **Y** in the *a* and *c* directions, respectively, and *a*, *c*, and β are the unit-cell parameters at the temperature and pressure of initial phase separation. To provide an exact phase boundary, vectors $\mathbf{Y}_1$ and $\mathbf{Y}_2$ must be equal in magnitude (Equation (3)):

$$|\mathbf{Y_1}| = |\mathbf{Y_2}| \quad (3)$$

Figure 11b shows a sketch of boundary orientations between lamellae and host with measured θ at ~11° from the *c* direction and the generic **Y** vector along the boundary.

Tribaudino et al. (2000) reported the cell parameters of Di_{100} and $Di_{80}En_{20}$ at different pressures. Following the approach of Zhao et al. (2017) and knowing that the composition of our sample is Di_{87} (diopside host) and Di_2 (clinoenstatite lamellae) [Di = 2×Wo = 2×Ca/(Ca+Mg+Fe+Mn); see Table 1], we calculated the cell parameters of our sample with interpolation by Equation (4).

$$a = a(\mathrm{Di}_{100}) - [\mathrm{a}(\mathrm{Di}_{100}) - \mathrm{a}(\mathrm{Di}_{80})]Q/20 \quad (4)$$

In this equation, *a* (or *c* or β) are the cell parameters Di_{87} or Di_2, and a(Di_{100}) and a(Di_{80}) are the cell parameters of Di_{100} and Di_{80}, respectively. $Q = 100 - 87 = 13$ for Di_{87}, and $Q = 100 - 2 = 98$ for Di_2. We list these cell parameters of our sample in Table 3 and plot them on Figure 12.

Setting $z = 1$, *x* can be calculated by

$$x = c\sin\theta\,/a\sin(180° - \theta - \beta) \quad (5)$$

where θ is the angle measured.

We calculate a series of values of *x* with different cell parameters at different pressures for the diopside host (Di_{87}) and clinoenstatite lamellae (Di_2) according to Equation (5) and calculate a series of values of **Y** for the diopside host (Di_{87}) and clinoenstatite lamellae (Di_2) according to Equations (1) or (2). All calculated data are listed in Table 4.

Because the vector **Y** is directed toward the acute angle β between the $-a$ and $+c$ directions, x should have a negative value when calculating **Y** by Equation (1) or (2).

From Table 4 we find that the difference between vector $\mathbf{Y_2}$ (host) and $\mathbf{Y_1}$ (lamellae) achieves a minimum at a pressure of 2 GPa, and we therefore suggest that the exsolution pressure of the lamellae at 10.68° to the c axis in the diopside host is ~2 GPa.

Zhao et al. (2017) analyzed the error associated with calculation of exsolution pressure, concluding that the boundary angle between the pyroxenes rather than their composition is the most critical parameter. They also conclude that accuracy in the measurement of this angle is crucial. Assuming the standard deviation (σ) on our mean angle measurements (0.36°), calculations for angles at 2σ from this mean (9.96º and 11.4º) give the same ~2 GPa result (Table 4), thus inferring that the error on the 2 GPa pressure estimate is 1 GPa or less.

Phase relationships - petrogenetic implications

The selection of pyroxene pairs shown in Fig. 1b includes examples from three distinct geological environments in which the phase associations, nanoscale characteristics such as spinodal decomposition, antiphase boundaries (APB), stacking faults, polymorph types and relative orientations of the two phases, can provide petrogenetic constraints in terms of *P*–*T*–*X*. The two pairs from UHP environments (Alpe Arami and Dabie terranes) plot close to the mantle xenoliths from the Mingxi terrane in terms of the exsolved phase, and just above the upper boundary of clinoenstatite and highest Mg composition (En component). In contrast, the two pairs from layered intrusions (Panzhihua and 'pigeonite I' from Bushveld) are close to one another in terms of the host (subcalcic diopside) and also show the highest Fe compositions (Fs component) for the exsolved phase. Using the geothermometer of Arlt et al. (2000) for *HT* Ca-poor clinopyroxene undergoing $C2/c$ to $P2_1/c$ transition relative to M2 site substitutions, the temperature estimated for Cen at Panzhihua is ~1030 ºC with a minimum $T \sim 810$ ºC (Table 5; Fig. 13a). Although the error on this thermometer is quite high, we have plotted, as Fig. 13a, for sake of comparison, the calculated M2 cation sizes relative to estimated T for all clinoenstatite/pigeonite occurrences with compositions given in Table 1b and

457 shown on Fig. 1b. The Cen from Panzhihua is closest to pigeonite from mantle xenoliths at Hannuoba
458 (Brizi et al. 2003) and with a calculated *T* in the middle of those considered here. In contrast, UHP
459 pigeonite from Dabieshan (Liu et al. 2007) and mantle xenoliths from Mingxi (Zhao et al. 2017) plot
460 at the upper end of the *T* range (~1170 to 1200 ºC), and the UHP pigeonite from Alpe Arami (Bozhilov
461 et al. 1999) are at the lower end of the range (~850 ºC). Temperatures for Bushveld pigeonite I (Boyd
462 and Brown 1969) are ~950 ºC, comparable with the ~1000 ºC obtained from exact phase boundary
463 geothermometry (Robinson et al. 1977). Considering pressures calculated for Panzhihua, *T* estimates
464 for subcalcic diopside (Di_{87}) (Table 1, Fig. 13b) using the geothermometer of Lindsley (1983) are
465 ~1050 ºC at 1 GPa, and ~1100 ºC at 2 GPa.

466 Despite differences in phase compositions (Fig. 1b), the Panzhihua and Hannuoba exsolution pairs
467 are also very similar in other ways, including evidence for spinodal decomposition and the
468 conspicuous lack of APBs. Brizi et al. (2003) discuss the exsolution invoking the (001) coherent
469 solvus and coherent spinodal of McCallister and Nord (1981), indicating *T* = ~1000 ºC at 1 atm for
470 an augite with Ca/(Ca+Mg) = 0.4. Nonetheless, considering the effect of pressure (~2 GPa) in
471 increasing *T* (Lindsley 1983), Brizi et al. (2003) conclude that exsolution took place at a minimum
472 temperature of ~1100 ºC and that the pigeonite lamellae initially formed via spinodal decomposition
473 before being coarsened during rapid transport to the surface. The observed spinodal exsolution of
474 (100) lamellae from subcalcic diopside with Ca/(Ca+Mg) = 0.5 from Panzhihua (Table 1a) cannot be
475 considered directly analogous and thus explained by a similar (001) coherent solvus – spinodal model
476 due to the lack of experimental constraints. Nonetheless, a similar mechanism as for Hannuoba, in
477 which rapid exsolution is followed by coarsening during upwards transport between reservoirs can
478 be invoked. This implies that exsolution conditions can be considered as T_{min} ~ 1050 ºC for Panzhihua
479 Cen. Brizi et al. (2003) explain the absence of APB domains in the pigeonite from Hannuoba by
480 considering their nucleation below the high-low pigeonite transition *T*, assuming such APBs are
481 associated with phase transition. An alternative explanation for the Panzhihua occurrence could,
482 however, relate to slower cooling rates/nucleation kinetics in layered intrusions relative to UHP

terranes or mantle-derived xenoliths rapidly ascending to the surface. No APBs are reported from the Bushveld occurrence despite the greater complexity in terms of lamellae sets.

We also speculate that the stress induced by titanomagnetite nucleation, following Cen exsolution, may have triggered formation of a second, much less well-developed set of pyroxene exsolutions (Fig. 2c, d). Titanomagnetite, present as epitaxial $[1\bar{1}0]$ lamellae within [010] diopside, is of the 'Z down' type (e.g., Fleet et al. 1980, and references therein) with lattice orientation $(111)_{Mt}$ // $(001)_{Di}$ and $(1\bar{1}\bar{1})_{Mt}$^$(100)_{Di}$ ~2–3°. The theory of optimal phase boundaries introduced for pyroxene–magnetite exsolutions (Fleet et al. 1980) with the purpose of developing reliable geothermobarometers could not be used due to the lack of two sets of titanomagnetite inclusions in the present samples.

Satellite reflections observed on different zone axes of magnetite in this study can be correlated with vacancy ordering models as suggested by Lattard (1995). Although double diffraction can be a factor, the fact that all recorded SAEDs show comparable 3-fold satellite reflections is evidence for considering them an intrinsic feature of Ti-free magnetite evolving towards ordered maghemite superstructures with tetragonal symmetry (Grau-Crespo et al. 2010). Sub-solidus diffusion of Fe^{2+} and Ti^{4+} atoms from the magnetite undergoing transformation towards maghemite within Trails 1 could source formation of ilmenite along the crosscutting Trails 2 (Fig. 6c–e). Such mechanisms could explain why the Ti-free domains appear darker on HAADF-STEM images (Fig. 7). The same conclusion is reached in the study by Tan et al. (2016) on Fe–Ti-oxides in the Panzhihua ores.

TEM studies of exsolution-derived microstructures in titanomagnetite resulting via spinodal decomposition show these evolve into 3-dimensional lamellar frameworks of ulvöspinel separating magnetite-enriched blocks, with secondary sets of exsolutions arising from ulvöspinel-rich domains (Price 1980). These features strongly resemble the fabrics (Trails 1 and 2; Fig. 6c–e) defined by domains with fine-exsolution of different orientations observed within titanomagnetite lamella (Fig. 7). Assemblages with exsolution textures between magnetite and ilmenite with scarce hercynite are also imaged and mapped at the nanoscale in mesostasis containing skeletal titanomagnetite from the Miller Range (MIL) 03346 Martian nakhlite meteorite (Righter et al. 2014). Compared to the

titanomagnetite reported here, however, these intergrowths are coarser and do not show the ultrafine-scale exsolutions present in our material from the Panzhihua intrusion.

The fine-scale textures and phase associations between clinopyroxenes and titanomagnetite are interpreted in terms of exsolution from high-*T* magmatic exsolution to low-*T* sub-solidus re-equilibration, as summarised in Figure 14.

Geological significance

The *P–T–X* data/estimates for exsolution pairs can be discussed in the context of the magma plumbing system proposed for the Emeishan LIP (Tao et al. 2015). Exsolution pressures of ~1.7–2 GPa, obtained for the clinopyroxene pairs from the gabbroic rocks at Panzhihua, correspond to a depth of ~40–56 km (assuming 1 kbar = 2.8 km; Tao et al. 2015). Such a depth would correspond to the level of the lowermost picrite reservoir in the model of Tao et al. (2015) (Fig. 15a). The temperature estimate for this magma is however >1500 ºC, far exceeding the T_{max} ~ 1100 ºC estimated here for pyroxene exsolution at 2 GPa (Fig. 13b). Constraints on the *P–T* exsolution of (100) Cen lamellae in the Panzhihua sample can be obtained by considering the data of Arlt et al. (2000) for the transition between space group *C*2/c and $P2_1/c$. Using the average cation size on the M2 site and the *HT* transition temperature, our low-Ca clinopyroxene underwent transition at about 1030 ºC, with a minimum of 810 ºC at 1 atm. for the composition $Wo_1En_{62}Fs_{37}$ (Fig 13a). The *HT*-transition temperature reported as 875–925 ºC at 1 atm (Cámara et al. 2002) is within this range. If we apply the average slope boundary (149 ºC/GPa) for the $P2_1/c$ – *HT* *C*2/*c* transition (Arlt et al. 2000), we obtain the transition line for Panzhihua shown on Fig. 15b. The intercept between this line and a vertical projection from *T*=1030 ºC at 1 atm for our Cen lamellae gives ~1.75 GPa as the maximum pressure at which the lamellae could have formed in space group *C*2/*c*. The intercept between the transition line for Panzhihua with a vertical projection from T_{max}=1100 ºC (obtained from Lindsley 1983) is just below 2 GPa. This *P–T* range represents a good fit with the ~2 GPa exsolution pressure calculated using the exact phase boundary theory and estimated *T* (Fig. 13).

The apparent contradiction between our results and the model for crustal–mantle architecture given by Tao et al. (2015) may suggest errors in that model, or in calculation of geothermal gradients. We also consider the possibility that the model presented by Tao et al. (2015) is fundamentally correct but that the clinopyroxene exsolution pairs analyzed here are relicts inherited from peridotites that may also have been present in the lowermost reservoir in the lower crust. We accept that such a hypothesis may not be supported by the chondrite-normalized REE fractionation patterns for pyroxene given by Gao et al. (2017). These data were, however, obtained from parts of the pyroxene grains outside the rare core domains that contained the exsolutions in order to avoid co-analysis of Fe–Ti-oxide inclusions. Although the pyroxenes may have undergone re-equilibration in the middle crust (high-Mg basaltic reservoir), they still preserve evidence for crystallization at greater depth. Such a hypothesis is indirectly supported by the similarity between our data and that from Hannuoba (Brizi et al. 2003), where spinel–peridotite nodules, occur in alkali basalts.

The hypothesis that the analyzed pyroxene pairs are relicts inherited from a deeper reservoir could also explain why such exsolution fields are restricted to specific parts of the pyroxene grains and are present only in some samples. Titanomagnetite crosscutting the pyroxene exsolutions could have formed in the same reservoir at T <1100 ºC with sequential sub-solidus sets of ilmenite + hercynite exsolutions at T <450 ºC (Price 1981). Such T estimates for titanomagnetite nonetheless require validation by methods such as the optimal phase boundary theory on suitable samples. Sequential petrologic–textural development of the assemblage (Fig. 15c–e) and the potential evolution from middle to upper crustal conditions is shown schematically by the arrow on Figure 14.

IMPLICATIONS

The present study shows clinopyroxene formed from gabbroic melts at Panzhihua displays multi-stage exsolutions and overprints not previously recognized. The crystal structural modifications interpreted for pyroxenes and magnetite within the assemblages can be further evidence for a protracted geological evolution as also concluded by Gao et al. (2017). Additional constraints on the

present interpretations could be obtained from estimation of temperature and pressures using phase boundary theory on samples containing two sets of titanomagnetite inclusions in clinopyroxene.

An increasing number of TEM studies focus on assemblages as those discussed here, but to our knowledge, only two other publications include atomic-scale HAADF-STEM imaging of the analyzed minerals: pyroxene (Kogure and Okunishi 2010); and magnetite (Xu et al. 2014). This is an emerging field of research (Ciobanu et al. 2016; Cook et al. 2017) and the present study shows how advanced electron microscopy, if focused on sites of petrogenetic interest, can provide challenging, new insights into ore deposit formation.

ACKNOWLEDGEMENTS

W.G. and F.H. acknowledge support from the National Natural Science Foundation of China (Grant No. 41272062), MLR Key Laboratory of Metallogeny and Mineral Assessment (Grant No. ZS1407), Key Laboratory of Earth and Planetary Physics (IGGCAS, Grant No. DQXX201706), and China Scholarship Council (Grants No. 201506080060 and 201606080020). CLC acknowledges support from the 'FOX' project (Trace elements in iron oxides), supported by BHP Olympic Dam and the South Australian Mining and Petroleum Services Centre of Excellence. N.J.C. acknowledges support from the ARC Research Hub for Australian Copper-Uranium. Additional microanalytical assistance was kindly provided by Animesh Basak and Ben Wade (Adelaide Microscopy). We acknowledge comments and enthusiastic discussion from Peter Robinson and Donald Lindsley on an earlier version of this manuscript, and the constructive input from two anonymous American Mineralogist reviewers.

REFERENCES CITED

Alvaro, M., Cámara, F., Domeneghetti, M.C., Nestola, F., and Tazzoli, V. (2011) *HT* $P2_1/c$ – $C2/c$ phase transition and kinetics of Fe^{2+}-Mg order-disorder of an Fe-poor pigeonite: Implications for the cooling history of ureilites. Contributions to Mineralogy and Petrology, 162, 599-613.

Angel, R.J., Chopelas, A., and Ross, N.L. (1992) Stability of high-density clinoenstatite at upper-mantle pressures. Nature, 358, 322-324.

584 Arlt, T., Angel, R.J., Miletich, R., Armbruster, T., and Peters, T. (1998). High-pressure $P2_1/c$-$C2/c$
585 phase transitions in clinopyroxenes: Influence of cation size and electronic structure. American
586 Mineralogist, 83, 1176-1181.
587 Arlt, T., Kunz, M., Stolz, J., Armbruster, T., and Angel, R.J. (2000) *P–T–X* data on $P2_1/c$
588 clinopyroxenes and their displacive phase transitions. Contributions to Mineralogy and Petrology,
589 138, 35-45.
590 Bollman, W. (1970) Crystal Defects and Crystalline Interfaces. Springer-Verlag, New York, 254 pp.
591 Bowles, J.F.W., Howie, R.A., Vaughan, D.J., and Zussman, J. (2011) Rock-forming Minerals: Non-
592 Silicates: Oxides, Hydroxides and Sulphides. The Geological Society of London, 920 pp.
593 Boyd, F.R., and Brown, G.M. (1969). Electron-probe study of pyroxene exsolution. Mineralogical
594 Society of America Special Paper, 2, 211-216.
595 Bozhilov, K.N., Green, H.W., and Dobrzhinetskaya, L. (1999) Clinoenstatite in Alpe Arami peridotite:
596 Additional evidence of very high pressure. Science, 284, 128-132.
597 Brizi, E., Nazzareni, S., Princivalle, F., and Zanazzi, F. (2003) Clinopyroxenes from mantle-related
598 xenocrysts in alkaline basalts from Hannuoba (China): Augite-pigeonite exsolutions and their
599 thermal significance. Contributions to Mineralogy and Petrology, 145, 578-584.
600 Brown, G.E., Prewitt, C.T., Papike, J.J., and Sueno, S. (1972) A comparison of the structures of low
601 and high pigeonite. Journal of Geophysical Research, 77, 5778-5789.
602 Buddington, A.F., and Lindsley, D.H. (1964) Iron-titanium oxide minerals and synthetic equivalents.
603 Journal of Petrology, 5, 310-357.
604 Buseck, P.R., Nord, G.L., and Veblen, D.R. (1980) Subsolidus phenomena in pyroxenes. Reviews in
605 Mineralogy and Geochemistry, 7, 117-211.
606 Cámara, F., Carpenter, M.A., Domeneghetti, M.C., and Tazzoli, V. (2002) Non-convergent ordering
607 and displacive phase transition in pigeonite: *in situ HT* XRD study. Physics and Chemistry of
608 Minerals, 29, 331-340.

609 Cameron, M., Shigeho, S., Prewitt, C.T., and Papike, J.J. (1973) High-temperature crystal chemistry
610 of acmite, diopside, hedenbergite, jadeite, spodumene, and ureyite. American Mineralogist, 58,
611 594-618.
612 Chisholm, J.E. (1982) Lowering of symmetry in pyribole structures. Mineralogical Magazine, 45, 25-
613 34.
614 Christy, A.G., and Angel, R.J. (1995) A model for the origin of the cell-doubling phase transitions in
615 clinopyroxene and the body-centred anorthite. Physics and Chemistry of Minerals, 22, 129-135.
616 Ciobanu, C.L., Cook, N.J., Utsunomiya, S., Pring, A., and Green, L. (2011) Focussed ion beam–
617 transmission electron microscopy applications in ore mineralogy: Bridging micro- and nanoscale
618 observations. Ore Geology Reviews, 42, 6-31.
619 Ciobanu, C.L., Cook, N.J., Maunders, C., Wade, B.P., and Ehrig, K. (2016) Focused ion beam and
620 advanced electron microscopy for minerals: Insights and outlook from bismuth sulphosalts.
621 Minerals, 6, 112; doi:10.3390/min6040112
622 Clark, J.R., Appleman, D.E., and Papike, J.J. (1969) Crystal-chemical characterization of
623 clinopyroxenes based on eight new structure refinements. Mineralogical Society of America
624 Special Paper, 2, 31-50.
625 Cook, N.J., Ciobanu, C.L., Ehrig, K., Slattery, A., Verdugo-Ihl, M.R., Courtney-Davies, L., and Gao,
626 W. (2017) Advances and opportunities in ore mineralogy. Minerals, 7, 233;
627 doi:10.3390/min7120233
628 Curtis, L., Gittins, J., Kocman, V., Rucklidge, J.C., Hawthorne, F.C., and Ferguson, R.B. (1975) Two
629 crystal structure refinements of a *P*2/*n* titanian ferro-omphacite. Canadian Mineralogist, 13, 62-67.
630 Doukhan, N., Ingrin, J., Doukhan, J.C., and Latrous, K. (1990) Coprecipitation of magnetite and
631 amphibole in black star diopside: A TEM study. American Mineralogist, 75, 840-846.
632 Feinberg, J.M., Wenk, H.R., Renne, P.R., and Scott, G.R. (2004) Epitaxial relationships of
633 clinopyroxene-hosted magnetite determined using electron backscatter diffraction (EBSD)
634 technique. American Mineralogist, 89, 462-466.

635 Ferraris, C., Folco, L., and Mellini, M. (2003) Sigmoidal exsolution by internal shear stress in
636 pyroxenes from chondritic meteorites. Physics and Chemistry of Minerals, 30, 503-510.
637 Fleet, M.E. (1981) The structure of magnetite. Acta Crystallographica Section B, 37, 917-920.
638 Fleet, M.E. (1986) The structure of magnetite: Symmetry of cubic spinels. Journal of Solid State
639 Chemistry, 62, 75-82.
640 Fleet, M.E., Bilcox, G.A., and Barnett, R.L. (1980) Oriented magnetite inclusions in pyroxenes from
641 the Grenville Province. Canadian Mineralogist, 18, 89-99.
642 Gao, W., Ciobanu, C.L., Cook, N.J., Huang, F., Meng, L., and Gao, S. (2017) Petrography and trace
643 element signatures in silicates and Fe–Ti-oxides from the Lanjiahuoshan deposit, Panzhihua
644 layered intrusion, Southwest China. Lithos, 294-295, 164-183.
645 Gasparik, T. (1990). A thermodynamic model for the enstatite-diopside join. American Mineralogist,
646 75, 1080-1091.
647 Grau-Crespo, R., Al-Baitai, A.Y., Saadoune, I., and Leeuw, N.H.D. (2010) Vacancy ordering and
648 electronic structure of γ-Fe_2O_3 (maghemite): A theoretical investigation. Journal of Physics:
649 Condensed Matter, 22, 255401-255407.
650 Haggerty, S.E. (1972) Apollo 14: Subsolidus reduction and compositional variations of spinels.
651 Proceedings of the Third Lunar Science Conference, 1, 305-332.
652 Haselton, J.C., and Nash, W.P. (1975) Ilmenite-orthopyroxene intergrowths from the moon and the
653 Skaergaard intrusion. Earth and Planetary Science Letters, 26, 287-291.
654 Hou, T., Zhang, Z.-C., and Pirajno, F. (2012) A new metallogenic model of the Panzhihua giant V–
655 Ti–iron oxide deposit (Emeishan Large Igneous Province) based on high-Mg olivine-bearing
656 wehrlite and new field evidence. International Geology Review, 54, 1721-1745.
657 Hugh-Jones, D.A., Woodland, A.B., and Angel, R.J. (1994) The structure of high-pressure *C*2/*c*
658 ferrosilite and crystal-chemistry of high-pressure *C*2/*c* pyroxenes. American Mineralogist, 79,
659 1032-1041.

660 Kitamura, M., Yasuda, M., and Morimoto, N. (1981) Morphology change of exsolution lamellae of
661 pigeonite in Bushveld augite - An electron-microscopic observation. Proceedings of the Japan
662 Academy Series B-Physical and Biological Sciences, 57, 183-187.
663 Kogure, T., and Okunishi, E. (2010) Cs-corrected HAADF-STEM imaging of silicate minerals.
664 Journal of Electron Microscopy, 59, 263-271.
665 Krasnova, N.I., and Krezer, Y.L. (1995). New data on the nature of fine and ultrafine lamellae in
666 titanomagnetite. European Journal of Mineralogy, 7, 1361-1372.
667 Lattard, D. (1995) Experimental evidence for the exsolution of ilmenite from titaniferous spinel.
668 American Mineralogist, 80, 968-981.
669 Lindsley, D.H. (1980). Phase equilibria of pyroxenes at pressures >1 atmosphere. Reviews in
670 Mineralogy and Geochemistry, 7, 289-307.
671 Lindsley, D.H. (1983). Pyroxene thermometry. American Mineralogist, 68, 477-493.
672 Liu, X.W., Jin, Z.M., and Green, H.W. (2007) Clinoenstatite exsolution in diopsidic augite of
673 Dabieshan: Garnet peridotite from depth of 300 km. American Mineralogist, 92, 546-552.
674 McCallister, R.H. (1978) The coarsening kinetics associated with exsolution in an iron-free
675 clinopyroxene. Contributions to Mineralogy and Petrology, 65, 327-331.
676 McCallister, R.H., and Nord, G.L. (1981). Subcalcic diopsides from kimberlites: Chemistry,
677 exsolution microstructures, and thermal history. Contributions to Mineralogy and Petrology, 78,
678 118-125
679 Moore, K.T., Elbert, D.C., and Veblen, D.R. (2001) Energy-filtered transmission electron microscopy
680 (EFTEM) of intergrown pyroxenes. American Mineralogist, 86, 814-825.
681 Morimoto, N., and Güven, N. (1970) Refinement of the crystal structure of pigeonite. American
682 Mineralogist, 55, 1195.
683 Mücke, A., 2003. Magnetite, ilmenite and ulvite in rocks and ore deposits: Petrography, microprobe
684 analyses and genetic implications. Mineralogy and Petrology, 77, 215-234.

685 Nakajima, Y., and Hafner, S.S. (1980) Exsolution in augite from the Skaergaard intrusion.
686 Contributions to Mineralogy and Petrology, 72, 101-110.
687 Pang, K.-N., Zhou, M.-F., Lindsley, D., Zhao, D.-G. and Malpas, J. (2008) Origin of Fe-Ti oxide ores
688 in mafic intrusions: Evidence from the Panzhihua Intrusion, SW China. Journal of Petrology, 49,
689 295-313.
690 Pang, K.-N., Li, C.-S., Zhou, M.-F., and Ripley, E.M. (2009) Mineral compositional constraints on
691 petrogenesis and oxide ore genesis of the late Permian Panzhihua layered gabbroic intrusion, SW
692 China. Lithos, 110, 199-214.
693 Pang, K.-N., Shellnutt, G.J., and Zhou, M.-F. (2015) The Panzhihua Intrusion, SW China. In B.
694 Charlier, O. Namur, R. Latypov, and C. Tegner, Eds. Layered Intrusions, p. 435-463. Springer
695 Netherlands, Dordrecht.
696 Pêcher, A., Arndt, N., Jean, A., Bauville, A., Ganino, C., and Athurion, C. (2013) Structure of the
697 Panzhihua intrusion and its Fe-Ti-V deposit, China. Geoscience Frontiers, 4, 571-581.
698 Price, G.D. (1980) Exsolution microstructures in titanomagnetites and their magnetic significance.
699 Physics of the Earth and Planetary Interiors, 23, 2-12.
700 Price, G.D. (1981) Subsolidus phase relations in the titanomagnetite solid solution series. American
701 Mineralogist, 66, 751-758.
702 Ramdohr, P. (1969) The Ore Minerals and their Intergrowths, English translation of the 3rd edition.
703 Pergamon Press, Oxford, 1174 pp.
704 Renne, P.R., Scott, G.R., Glen, J.M.G., and Feinberg, J.M. (2002) Oriented inclusions of magnetite
705 in clinopyroxene: Source of stable remanent magnetization in gabbros of the Messum Complex,
706 Namibia. Geochemistry, Geophysics, Geosystems, 3, 1-11.
707 Righter, K., Keller, L.P., Rahman, Z., and Christoffersen, R. (2014) Redox-droven exsolution of iron-
708 titanium oxides in magnetite in Miller range (MIL) 03346 nakhlite: Evidence for post
709 crystallization oxidation in the nakhlite cumulate pile? American Mineralogist, 99, 2313-2319.

Robinson, P., Jaffe, H.W., Ross, M., and Klein, C., Jr. (1971) Orientation of exsolution lamellae in clinopyroxenes and clinoamphiboles; consideration of optimal phase boundaries. American Mineralogist, 56, 909-939.

Robinson, P., Ross, M., Nord, G.L., Smyth, J.R., and Jaffe, H.W. (1977) Exsolution lamellae in augite and pigeonite: Fossil indicators of lattice-parameters at high-temperature and pressure. American Mineralogist, 62, 857-873.

Shannon, R.D. (1976) Revised effective ionic radii and systematic studies of interatomic distances in halides and chalcogenides. Acta Crystallographica Section A, 32, 751-767.

Shellnutt, J., and Jahn, B.-M. (2010) Formation of the Late Permian Panzhihua plutonic-hypabyssal-volcanic igneous complex: implications for the genesis of Fe–Ti oxide deposits and A-type granites of SW China. Earth and Planetary Science Letters, 289, 509-519.

Song, X.-Y., Qi, H.-W., Hu, R.-Z., Chen, L.-M., Yu, S.-Y., and Zhang, J.-F. (2013) Formation of thick stratiform Fe-Ti oxide layers in layered intrusion and frequent replenishment of fractionated mafic magma: Evidence from the Panzhihua intrusion, SW China. Geochemistry, Geophysics, Geosystems, 14, 712-732.

Tan, W., Liu, P., He, H., Wang, C.Y., and Liang, X. (2016). Mineralogy and origin of exsolution in Ti-rich magnetite from different magmatic Fe-Ti oxide-bearing intrusions. The Canadian Mineralogist, 54, 539-553.

Tao, Y., Putirka, K., Hu, R.-Z., and Li, C. (2015) The magma plumbing system of the Emeishan large igneous province and its role in basaltic magma differentiation in a continental setting. American Mineralogist, 100, 2509-2517.

Tribaudino, M., Prencipe, M., Bruno, M., and Levy, D. (2000) High-pressure behaviour of Ca-rich $C2/c$ clinopyroxenes along the join diopside-enstatite ($CaMgSi_2O_6$-$Mg_2Si_2O_6$). Physics and Chemistry of Minerals, 27, 656-664.

Tribaudino, M., Nestola, F., Cámara, F., and Domeneghetti, M.C. (2002) The high-temperature $P2_1/c$ - $C2/c$ phase transition in Fe-free pyroxene ($Ca_{0.15}Mg_{1.85}Si_2O_6$): Structural and thermodynamic behavior. American Mineralogist, 87, 648-657.

Tribaudino, M., Nestola, F., Meneghini, C., and Bromiley, G.D. (2003) The high-temperature $P2_1/c$ – $C2/c$ phase transition in Fe-free Ca-rich $P2_1/c$ clinopyroxenes. Physics and Chemistry of Minerals, 30, 527-535.

Verwey, E.J.W., and de Boer, J.H. (1936) Cation arrangement in a few oxides with crystal structures of the spinel type. Recueil des Travaux Chimiques des Pays Bas, 55, 531-540.

Wang, Z.M., Yang, Q.B., and Kuo, K.H. (1989) Description of hexagonal Frank-Kasper phases by a projection method. Acta Crystallographica Section A, 45, 268-274.

Woensdregt, C.F., Weibel, M., and Wessicken, R. (1983) Electron microscopical investigation of oriented magnetite and amphibole in black star diopside. Schweizerische mineralogische und petrographische Mitteilungen, 63, 167-176.

Woodland, A.B., and Angel, R.J., 1997. Reversal of the orthoferrosilite-high-P clinoferrosilite transition, a phase diagram for $FeSiO_3$ and implications for the mineralogy of the Earth's upper mantle. European Journal of Mineralogy, 9, 245-254.

Xing, C.-M., and Wang, C.Y. (2017) Cathodoluminescence images and trace element compositions of fluorapatite from the Hongge layered intrusion in SW China: A record of prolonged crystallization and overprinted fluid metasomatism. American Mineralogist, 102, 1390-1401.

Xu, H.-F., Shen, Z.-Z., and Konishi, H. (2014) Si-magnetite nano-precipitates in silician magnetite from banded iron formation: Z-contrast imaging and ab initio study. American Mineralogist, 99, 2196-2202.

Zhao, S.R., Zhang, G.G., Sun, H., Mason, R., and He, X. (2017) Orientation of exsolution lamellae in mantle xenolith pyroxenes and implications for calculating exsolution pressures. American Mineralogist, 102, 2096-2105.

759 Zhou, M.-F., Robinson, P.T., Lesher, C.M., Keays, R.R., Zhang, C.-J., and Malpas, J. (2005)
760 Geochemistry, petrogenesis and metallogenesis of the Panzhihua gabbroic layered intrusion and
761 associated Fe–Ti–V oxide deposits, Sichuan Province, SW China. Journal of Petrology, 46, 2253-
762 2280.

763 **FIGURE CAPTIONS**

764 **FIGURE 1.** (a) Wollastonite (Wo) – enstatite (En) – ferrosilite (Fs) compositional triangle showing the
765 compositional space for pyroxenes below the diopside (Di) – hedenbergite (Hd) tie-line. Augite and
766 pigeonite solid solutions are linked by dashed lines schematically showing the resulting exsolution pairs
767 (adapted from Lindsley 1980). (b) Di–Hd–En–Fs plot showing the composition of clinopyroxene pairs from
768 Panzhihua and examples from the literature as marked (compositions from Table 1a, b). (c, d) BSE images
769 showing the position of EPMA spots (red circles) and FIB cuts from which TEM foils were prepared. Grey
770 area represents the EPMA composition obtained from the profile marked in (c, d). Composition of Cen
771 lamella is obtained using geometrical relationships within Wo–En–Fs compositional space. Abbreviations:
772 Amph – amphibole; Fe–Ti-ox – Fe–Ti-oxides; Ol – olivine.

773 **FIGURE 2.** Low-magnification HAADF-STEM (a, b) and BF TEM (c–e) images of the two foils showing
774 exsolution lamellae of clinoenstatite and titanomagnetite (narrow, diagonal) within host diopside. Note
775 lamellae branching/splitting in (c–e) indicative of spinodal decomposition. Abbreviations: Cen –
776 clinoenstatite; Ti-Mt – titanomagnetite

777 **FIGURE 3.** SAEDs of clinopyroxene lamellae (clinoenstatite; Cen) and host (diopside; Di) down to zone axes
778 as marked. The electron diffractions (beam illuminated area ~200 nm) are obtained from diopside without
779 lamellae (a), on top of a lamella (b and d), and at the boundary between the two (c). SAEDs in (b) and (c)
780 show satellite reflections corresponding to clinoenstatite (marked in yellow). Inset in (c) shows rotation on
781 satellite reflections (arrowed) along a^* indicative of modulation attributable to spinodal decomposition. In
782 (d), the two phases are undistinguishable and the SAED shows *h0l*, with h, $l \neq 2n$ reflections (red circle)
783 violating the symmetry for $C2/c$ and $P2/c$ space groups corresponding to diopside and clinoenstatite,
784 respectively. See text for further explanation.

FIGURE 4. (a) HAADF-STEM image of clinoenstatite (Cen) lamella in diopside (Di) obtained from a very thin area at the top of Foil 1. Dark spots (diameter ~5 nm) are produced by beam damage during EDS analysis. Note larger spots for host than lamella due to the Ca amount. (b) Fast Fourier Transform (FFT) obtained from image in (a) showing orientation of pyroxenes on [010] zone axis. The index (801) for lattice plane orientation for diopside relative to the lamella is obtained at the intercept between a^* rotated at measured θ (~11º) and (*h02*; *h=2n*) lattice vector. This orientation is schematically shown in Figure 2c. (c–d) Selected EDS spectra for lamella and host, respectively. The Cu signal derives from the TEM grid. Note Fe content is higher in the lamella explaining the brighter color on the HAADF-STEM images.

FIGURE 5. High-resolution HAADF-STEM images viewed down to *b* axis in the pyroxenes showing the interface between the two phases (a), and a detail of atomic arrangement in clinoenstatite (b). Note the images show the difference between the crystal symmetry of the two pyroxenes by the spacings between the bright atom arrays along the *a* axis, i.e., intervals with two distinct widths in clinoenstatite as opposed to single width interval in diopside. Phase boundary relationships and measurement of θ ~10º is marked on (a). (c) Inverse Fast Fourier Transform (IFFT) image obtained from HAADF-STEM image in (b). Structure model for clinoenstatite (d) and diopside (e) down to the *b* axis. This shows that the brightest atoms correspond to cations (Mg, Fe, Ca) in octahedral coordination sandwiched between the SiO_4 tetrahedra. Silicon atoms are represented by the less-bright atoms.

FIGURE 6. HAADF-STEM images (a–h) and EDS spectra (i) of phases within the titanomagnetite (Ti-Mt) lamella. (a) Slight displacement between the clinoenstatite (Cen; arrowed) lamellae at the boundary with the Ti-Mt indicative of two stages of exsolutions from host diopside (Di). (b–d) Two crosscutting trails with fine-intergrowths of different phases (variable contrast on the images) are present throughout the Ti-Mt lamella. (d) Fine substructures in Trails 1 show different orientation to one another in the middle part of the grain where a Cen lamella crosscuts Ti-Mt. The crosscutting pyroxene is partially altered to chlorite (Chl). In detail, phases along Trails 2 consist of spinel (Spl) and ilmenite grains (Ilm) (c, e). (f) Phases identified at the junction between the two trails include: magmetite (Mt), Ilm, Spl and Ti-Mt. (g) Relationships between Spl, Ilm and Mt along Trails 1. (h) Boundary between Ilm and Mt along Trails 1 showing atom arrays in the two phases with parallel orientation to one another. (i) EDS spectra for Ti-Mt, Mt, Ilm and Spl (as marked), obtained from the thinner areas (white circles). The Cu signal is from the grid.

FIGURE 7. (a) HAADF-STEM image and (b) STEM EDS element map overlapping Ti (blue), Al (red) and Mg (green) obtained from the middle-lower part of the titanomagnetite lamella. In (b) the lamella shows two domains defined by sub-structures within the wider strips (Trails 1) with finer exsolutions of different orientation relative to the strip boundaries. Note the darker color of magnetite strips which are free of exsolved phases. Abbreviations: Cen – clinoenstatite; Di – diopside; Her – hercynite; Ilm – ilmenite; Mgm – maghemite; Mt – magnetite; Ti-Mt – titanomagnetite.

FIGURE 8. SAEDs representing magnetite on zone axes as marked (a–e). (f) Bright Field (BF) TEM image showing location of SAED in (e) along the titanomagnetite lamella. Note satellite reflections (arrowed) in (a) and (c–e). SAEDs on $[1\bar{1}0]$ zone axis display (00l), *l=2n* reflections (red circle) violating the *Fd*3*m* symmetry and are indexed using $F\bar{4}3m$ space group (b, d). (e) Satellite reflections along $(\bar{2}\bar{2}2)$ and parallel rows in magnetite can be indexed using ilmenite with *P*6/*m* space group. Abbreviations: Mt – magnetite; Ilm – ilmenite.

FIGURE 9. (a–e) High-resolution HAADF-STEM images of phases within the titanomagnetite lamella with the specimen tilted down to $[\bar{1}10]$ zone axis. (a) Sharp boundaries between spinel (Spl) and magnetite (Mt). (b) Triple junction among spinel, magnetite and ilmenite (Ilm). (c, d) Stepwise atomic arrangements along the boundaries between magnetite and ilmenite. Insets in (d) are FFTs for magnetite and ilmenite. (e) Atomic arrangement in magnetite down to the $[\bar{1}10]$ zone axis. Note the presence of bright, larger atoms surrounded by a ring of smaller, less bright atoms. (f) Inverse FFT obtained from an area in (e) with the rhombus motif defining the lattice on $[\bar{1}10]$ highlighted by 9 brightest atoms marked by yellow circles. (f, g) Crystal structure models of magnetite on $[\bar{1}10]$ using $F\bar{4}3m$ and *Fd*3*m* space groups, respectively. Oxygen atoms are ignored. The brightest atoms correspond to Fe in tetrahedral coordination marked as Fe1 and FeA in (g) and (h). The less-bright atoms correspond to FeB (h) and Fe2, Fe3 (g) in octahedral coordination. The images in (e, f) show a better fit to the model in (g) as the less bright atoms form a slightly asymmetric circle around the brightest atoms.

FIGURE 10. HAADF-STEM images showing the amphibole (Amph) along the boundary between the titanomagnetite lamellae and pyroxene (a, c–f) and EDS spectra for amphibole (b); compare with EDS spectra for pyroxenes in Figure 3b, c. (c) Disordered brighter strips in amphibole. (d) Amphibole lamella protruding into magnetite (Mt). (e) Sharp boundaries between magnetite and diopside (Di). Note (111) in

Mt is parallel to *c* in Di. (f) Scalloped boundary between amphibole and magnetite suggestive of replacement relationships.

FIGURE 11. (a) 3D schematic showing the crystallographic orientation of lamella within the observed space (represented by the cube). The crystallographic axes are set for lamella as shown. (b) Sketch of boundary orientation between lamellae and host in clinopyroxenes. Relationships between cell parameters for lamella and host correspond to data interpolated from Figure 12 and tabulated in Table 3 for a pressure of 1 GPa. The vector '**Y**' along the boundary is schematically shown for a best fit between $\mathbf{Y_1}$ and $\mathbf{Y_2}$ of the two phases. Notation of 1 (lamella) and 2 (host) correspond to equations (1) – (3) in the text. Angle θ corresponds to measurements given in Table 2.

FIGURE 12. Plot of cell parameters and β *vs.* pressure for Di_{100} and Di_{80} (Tribaudino et al. 2000), and for Di_{87} and Di_2 (this paper). Data compiled in Table 3. Abbreviation: Di – diopside.

FIGURE 13. Temperature estimates for Panzhihua exsolutions and examples from the literature (see text). (a) Transition temperatures in $P2_1/c$ clinopyroxene as a function of the average M2-octahedral site at 1 atm (data in Table 5) from Figure 5 in Arlt et al. (2000). Dashed lines represent the error relative to the correlation between M2 size and *T* (full line). (b) Phase diagram calculated for the join diopside–enstatite at 2 GPa showing composition versus temperature after Lindsley (1980). Temperature estimates for Panzhihua and Hannuoba are derived using compositions of host subcalcic diopside and subcalcic augite, respectively (Table 1a, b). The drop in *T* at 1 GPa is also shown for Panzhihua (diagram from Lindsley 1980).

FIGURE 14. Schematic illustration of the sequential development of textures among pyroxenes, Fe–Ti-oxides and related phases from initial, high-*T* exsolution of clinoenstatite and titanomagnetite, through sub-solidus Fe–Ti-phase re-equilibration, to post-magmatic overprinting. See text for additional explanation.

FIGURE 15. (a) Schematic reconstruction of proposed magma chamber evolution and plumbing at Panzhihua, modified from Tao et al. (2015) with successive textural stages marked as c–e. We suggest the presence of peridotite magma at depth (light green, just close to the lithospheric mantle) as a deeper reservoir from which the present pyroxene with sequential exsolutions may have been inherited. (b) Plot of temperature *vs.* pressure, adapted from Arlt et al. (2000). The triple joint for the phase boundary between *Pbca*, *HP C*2/*c* and $P2_1/c$ for $Mg_{0.9}Fe_{0.1}SiO_3$ (dotted; extrapolated from Woodland and Angel 1997) is shifted ~2 GPa towards lower pressure (solid line; Arlt et al. 2000). Phase boundary $P2_1/c$ – *HT C*2/*c* is drawn by using *T*

870 at 1 bar relative to M2 size and a slope of ~149 °C/GPa. Blue dashed line: Alpe Arami and Hannuoba
871 pigeonite at T_{min} ~ 850 °C. Red dashed line Panzhihua clinoenstatite at T_{min} ~ 810 °C (this work). Red dotted
872 lines are drawn to show the corresponding pressures for T ~ 1030 °C estimated at 1 bar and T_{max} ~ 1100 °C
873 at 2 GPa (according to Fig. 13a and b, respectively). Red circle represents estimated exsolution conditions
874 for pyroxene pairs from Panzhihua (~1.7–2 GPa, 1030–1100 °C) across the $P2_1/c$ – *HT* $C2/c$ phase
875 transition. (c–e) Sequential petrologic–textural development of the assemblage from lower to upper crustal
876 conditions.

TABLE 1a. EPMA[1] data for subcalcic diopside host and estimated composition of clinoenstatite lamellae in the exsolution field

wt%.	1	2	3	4	5	6	7	Mean (n=7)	Lamellae (estimated)
SiO_2	51.07	50.96	50.94	51.04	50.90	50.99	50.82	50.96	53.00
TiO_2	1.24	1.29	1.23	1.23	1.22	1.18	1.23	1.23	0.10
Al_2O_3	3.18	3.08	3.07	3.15	3.09	3.11	3.11	3.11	0.40
FeO^T	8.09	8.09	8.81	8.28	7.67	8.28	7.90	8.16	23.59
Fe_2O_3	2.26	2.43	2.49	2.19	1.71	2.45	2.16	2.24	0.01
FeO	6.05	5.90	6.57	6.31	6.14	6.08	5.96	6.14	23.58
MnO	0.28	0.25	0.29	0.21	0.29	0.25	0.23	0.26	0.02
MgO	14.74	14.63	15.24	14.85	14.67	14.94	14.63	14.81	22.00
CaO	21.12	21.24	19.99	20.75	21.15	20.70	21.31	20.89	0.50
Na_2O	0.54	0.57	0.52	0.55	0.49	0.55	0.51	0.53	0.00
P_2O_5	0.00	0.00	0.00	0.00	0.00	0.00	0.04	0.01	0.00
Total	100.49	100.35	100.31	100.28	99.66	100.25	100.00	100.19	99.61
Number of ions on the basis of 6 (O)									
Al	0.023	0.017	0.017	0.024	0.027	0.021	0.020	0.021	0.006
Ti	0.035	0.036	0.034	0.034	0.034	0.033	0.034	0.034	0.003
Fe^{3+}	0.063	0.068	0.069	0.061	0.048	0.068	0.060	0.062	0.000
Mg	0.811	0.806	0.840	0.818	0.813	0.823	0.809	0.817	1.230
Fe^{2+}	0.187	0.182	0.203	0.195	0.191	0.188	0.185	0.190	0.740
Mn	0.009	0.008	0.009	0.007	0.009	0.008	0.007	0.008	0.001
Ca	0.835	0.841	0.792	0.822	0.842	0.820	0.847	0.828	0.020
Na	0.039	0.041	0.037	0.040	0.035	0.039	0.037	0.038	0.000
P	0.000	0.000	0.000	0.000	0.000	0.000	0.001	0.000	0.000
Total	2.000	1.999	2.000	2.000	2.000	2.000	2.000	2.000	2.000
Si	1.884	1.883	1.883	1.887	1.892	1.885	1.884	1.886	1.988
Al	0.116	0.117	0.117	0.113	0.108	0.115	0.116	0.114	0.012
Total	2.000	2.000	2.000	2.000	2.000	2.000	2.000	2.000	2.000
Calculated end-members									
En	42.6	42.3	43.9	43.0	42.7	43.2	42.4	42.9	61.8
Fs	13.6	13.5	14.7	13.8	13.0	13.8	13.2	13.7	37.2
Wo	43.9	44.2	41.4	43.2	44.3	43.0	44.4	43.5	1.0
Di	87.7	88.3	82.8	86.4	88.5	86.0	88.8	86.9	2.0

Notes: FeO and Fe_2O_3 values were calculated from FeO^T. En = 100×Mg/(Mg+Fe*+Ca); Fs=100×Fe*/(Mg+Fe*+Ca); Wo=100×Ca/(Mg+Fe*+Ca); Di=2×Wo; $Fe^*=Fe^{2+}+Fe^{3+}+Mn$

Reference: [1] Gao et al. (2017)

This is a preprint, the final version is subject to change, of the American Mineralogist (MSA)
Cite as Authors (Year) Title. American Mineralogist, in press.
DOI: https://doi.org/10.2138/am-2019-6764

TABLE 1b. EPMA data for augite/diopside host and estimated composition of enstatite/pigeonite lamellae in the exsolution field given in the discussed published studies

	Mingxi [1]		Dabie [2]		Hannuoba [3]		Bushveld [4]		Alpe Arami [5]	
	Host	Lamella	Host	Lamella	Host	Lamella	Host	Lamella	Host	Lamella
wt%	diopside ("Cpx-host")	enstatite/ pigeonite ("Opx lamella in Cpx host")	augite ("Cpx mantle")	clinoenstatite (EDS)	subcalcic augite ("mean C5-C10 TEM-EDS")	pigeonite ("mean C5-C10 TEM-EDS")	augite	Pigeonite I (clino-hypersthene)	diopside	clinoenstatite
SiO_2	52.85	55.89	55.50	57.50	50.30	54.42	51.80	52.20	54.62	56.95
TiO_2	0.18	0.03	0.00	n.a.	n.a	n.a.	0.50	0.20	0.36	n.a.
Al_2O_3	6.48	4.48	3.26	n.a.	8.48	4.64	1.52	0.85	0.93	0.48
FeO^T	2.33	6.01	3.46	5.50	8.09	13.18	10.80	25.60	3.59	8.85
Fe_2O_3	0.00	0.00	0.00	n.a.	0.00	0.00	0.58	0.00	n.a.	n.a.
FeO	2.33	6.01	3.46	n.a.	8.09	13.18	10.27	25.60	n.a.	n.a.
MnO	0.08	0.12	0.00	n.a.	n.a.	n.a.	0.30	0.60	n.a.	n.a.
MgO	14.28	29.77	22.53	33.17	14.64	21.32	13.30	19.60	15.39	29.99
CaO	20.99	3.78	13.34	3.22	18.51	6.45	21.20	0.80	23.96	3.72
Na_2O	1.74	0.31	0.79	n.a.	n.a	n.a.	0.20	0.05	0.85	n.a.
P_2O_5	n.a.	n.a.	0.00	n.a.	n.a	n.a.	n.a.	n.a.	n.a.	n.a.
Total	98.93	100.38	98.88	99.38	100.00	100.01	99.68	99.90	99.70	100.00
Number of ions on the basis of 6 (O)										
Al	0.190	0.116	0.020	n.a.	0.219	0.186	0.018	0.017	0.040	0.020
Ti	0.005	0.001	0.034	n.a.	n.a.	n.a.	0.014	0.036	0.010	n.a.
Fe^{3+}	0.000	0.000	0.060	n.a.	0.000	0.000	0.017	0.068	n.a.	n.a.
Mg	0.771	1.535	0.809	1.720	0.803	1.160	0.747	0.806	0.840	1.570
Fe^{2+}	0.071	0.173	0.185	0.140	0.247	0.397	0.324	0.182	0.080	0.250
Mn	0.002	0.003	0.007	n.a.	n.a.	n.a.	0.010	0.008	n.a.	n.a.
Ca	0.814	0.140	0.847	0.120	0.730	0.252	0.855	0.841	0.940	0.140
Na	0.122	0.021	0.037	n.a.	n.a.	n.a.	0.015	0.041	0.060	n.a.
P	n.a.	n.a.	0.001	n.a.	n.a.	n.a.	n.a.	n.a.	n.a.	n.a.
Total	1.975	1.990	2.000	1.980	1.999	1.994	1.999	1.999	1.970	1.980
Si	1.914	1.933	1.884	2.000	1.851	1.986	1.951	1.980	2.000	2.000
Al	0.086	0.067	0.116	n.a.	0.149	0.014	0.049	0.020	n.a.	n.a.
Total	2.000	2.000	2.000	2.000	2.000	2.000	2.000	2.000	2.000	2.000
Calculated end-members										
En	46.5	82.9	66.2	86.9	45.1	64.1	38.3	56.2	45.2	80.1
Fs	4.4	9.5	5.7	7.1	13.9	21.9	17.9	42.1	4.3	12.8
Wo	49.1	7.6	28.2	6.1	41.0	13.9	43.8	1.6	50.5	7.1
Di	98.2	15.1	56.3	12.1	82.0	27.9	87.7	3.3	101.1	14.3

Notes: FeO and Fe_2O_3 values were calculated from FeO^T. En = 100×Mg/(Mg+Fe*+Ca); Fs=100×Fe*/(Mg+Fe*+Ca); Wo=100×Ca/(Mg+Fe*+Ca); Di=2×Wo; Fe*=Fe^{2+}+Fe^{3+}+Mn; n.a. no analysis; Cpx – clinopyroxene; Opx – orthopyroxene

References: [1] Zhao et al. (2017); [2] Liu et al. (2007); [3] Brizi et al. (2003); [4] Robinson et al. (1977) using data of Boyd and Brown (1969); [5] Bozhilov et al. (1999)

TABLE 2. Measurements of the pyroxene phase interface orientation

Image type	Image no.	Angle (°)
HAADF STEM	170825-1_0006	10.16
n=8	170825-1_0006	10.16
	170825-1_0004	10.22
	170825-1_0008	10.52
	170825-1_0004	10.72
	170825-1_0018	10.89
	170825-1_0018	10.89
	170825-1_0008	10.99
	Mean	10.57
	σ	0.35
BF TEM	170822-35	10.49
n=4	170822-31	10.78
	170822-18	11.04
	170822-20	11.24
	Mean	10.89
	σ	0.33
Combined	Mean	10.68
n=12	σ	0.36

TABLE 3. Cell parameters of diopside host (Di_{87}) and clinoenstatite lamellae (Di_2)

P (GPa)	Host (Di_{87})			Lamellae (Di_2)		
	a (Å)	*c* (Å)	*β* (°)	*a'* (Å)	*c'* (Å)	*β'* (°)
1	9.7083	5.2334	106.011	9.6445	5.2291	107.456
2	9.6783	5.2154	105.839	9.6145	5.1984	106.944
3	9.6526	5.1991	105.690	9.5973	5.1736	106.540
4	9.6330	5.1868	105.577	9.5607	5.1528	106.469
5	9.6084	5.1723	105.448	9.5064	5.1085	105.958
6	9.5873	5.1589	105.329	9.5108	5.0994	105.584
7	9.5673	5.1469	105.223	9.5035	5.1001	105.308
8	9.5483	5.1369	105.144	9.4845	5.0901	104.974
9	9.5290	5.1266	105.085	9.4567	5.0713	104.787

This is a preprint, the final version is subject to change, of the American Mineralogist (MSA)
Cite as Authors (Year) Title. American Mineralogist, in press.
DOI: https://doi.org/10.2138/am-2019-6764

TABLE 4. *x* and **Y** at different pressures for diopside host (Di_{87}) and clinoenstatite lamellae (Di_2)

Angle	P (GPa)	Host (Di_{87})		Lamellae (Di_2)		$\lvert\mathbf{Y_1}\rvert$–$\lvert\mathbf{Y_2}\rvert$ (Å)
		x	$\lvert\mathbf{Y_2}\rvert$ (Å)	x'	$\lvert\mathbf{Y_1}\rvert$ (Å)	
10.68°	1	0.11182	5.63030	0.11394	5.65674	0.02645
	2	0.11161	5.60735	0.11309	5.61251	0.00516
	3	0.11141	5.58670	0.11234	5.57715	-0.00955
	4	0.11127	5.57112	0.11225	5.55324	-0.01788
	5	0.11112	5.55282	0.11141	5.49488	-0.05794
	6	0.11096	5.53603	0.11080	5.47739	-0.05863
	7	0.11083	5.52091	0.11064	5.47250	-0.04841
	8	0.11076	5.50856	0.11033	5.45498	-0.05358
	9	0.11071	5.49630	0.11008	5.43107	-0.06524
11.40° (mean+2σ)	1	0.12003	5.66654	0.12236	5.69546	0.02892
	2	0.11980	5.64318	0.12143	5.65011	0.00693
	3	0.11958	5.62217	0.12061	5.61388	-0.00829
	4	0.11942	5.60631	0.12051	5.58970	-0.01661
	5	0.11925	5.58770	0.11959	5.53017	-0.05753
11.04° (mean+1σ)	1	0.11591	5.64825	0.11814	5.67592	0.02767
	2	0.11569	5.62510	0.11725	5.63114	0.00604
	3	0.11548	5.60427	0.11646	5.59535	-0.00892
	4	0.11533	5.58855	0.11636	5.57130	-0.01725
	5	0.11517	5.57010	0.11549	5.51236	-0.05774
10.32° (mean-1σ)	1	0.10775	5.61268	0.10978	5.63791	0.02523
	2	0.10755	5.58994	0.10897	5.59423	0.00429
	3	0.10737	5.56947	0.10825	5.55930	-0.01017
	4	0.10723	5.55401	0.10816	5.53551	-0.01850
	5	0.10708	5.53587	0.10736	5.47772	-0.05814
9.96° (mean-2σ)	1	0.10371	5.59539	0.10564	5.61942	0.02403
	2	0.10352	5.57285	0.10487	5.57628	0.00343
	3	0.10334	5.55255	0.10418	5.54177	-0.01078
	4	0.10321	5.53723	0.10410	5.51811	-0.01912
	5	0.10308	5.51924	0.10334	5.46089	-0.05835

This is a preprint, the final version is subject to change, of the American Mineralogist (MSA)
Cite as Authors (Year) Title. American Mineralogist, in press.
DOI: https://doi.org/10.2138/am-2019-6764

TABLE 5. Composition and size of M2 cation and estimated temperature for pigeonite/enstatite lamellae in Table 1 using the geothermometer of Arlt et al. (2000)

M2*	Panzhihua (this study)	Mingxi	Dabie	Hannuoba	Bushveld	Alpe Arami
Mg	0.230	0.535	0.720	0.209	0.108	0.570
Fe	0.740	0.173	0.140	0.372	0.812	0.250
Ca	0.020	0.140	0.120	0.209	0.033	0.140
Al^{VI}		0.116		0.204	0.018	0.020
Na		0.021			0.004	0.030
Mn					0.019	
Total	0.990	0.985	0.980	0.994	0.994	1.010
Calculated effective M2 cation size (Å) using cation radii from Shannon (1976)						
Mg	0.166	0.385	0.518	0.150	0.078	0.410
Fe	0.577	0.135	0.109	0.290	0.633	0.191
Ca	0.020	0.140	0.120	0.209	0.033	0.140
Al^{VI}		0.062		0.109	0.010	0.011
Na		0.021			0.004	0.031
Mn					0.016	
Total	0.763	0.744	0.748	0.759	0.774	0.783
Estimated temperature read from Fig. 13a (°C)						
T	1030	1200	1170	1100	950	850
T_{min}	810	955	925	850	720	650

* Site M2 was filled to sum 1.00 with remaining Mg^{2+}, Fe^{2+}, Mn^{2+} as well as Ca^{2+} and Na^{+} after filling site M1 to sum to 1,00 with cations in the order: Al^{3+}, Fe^{3+}, Mg^{2+}, Fe^{2+}, Mn^{2+}.

This is a preprint, the final version is subject to change, of the American Mineralogist (MSA)
Cite as Authors (Year) Title. American Mineralogist, in press.
DOI: https://doi.org/10.2138/am-2019-6764

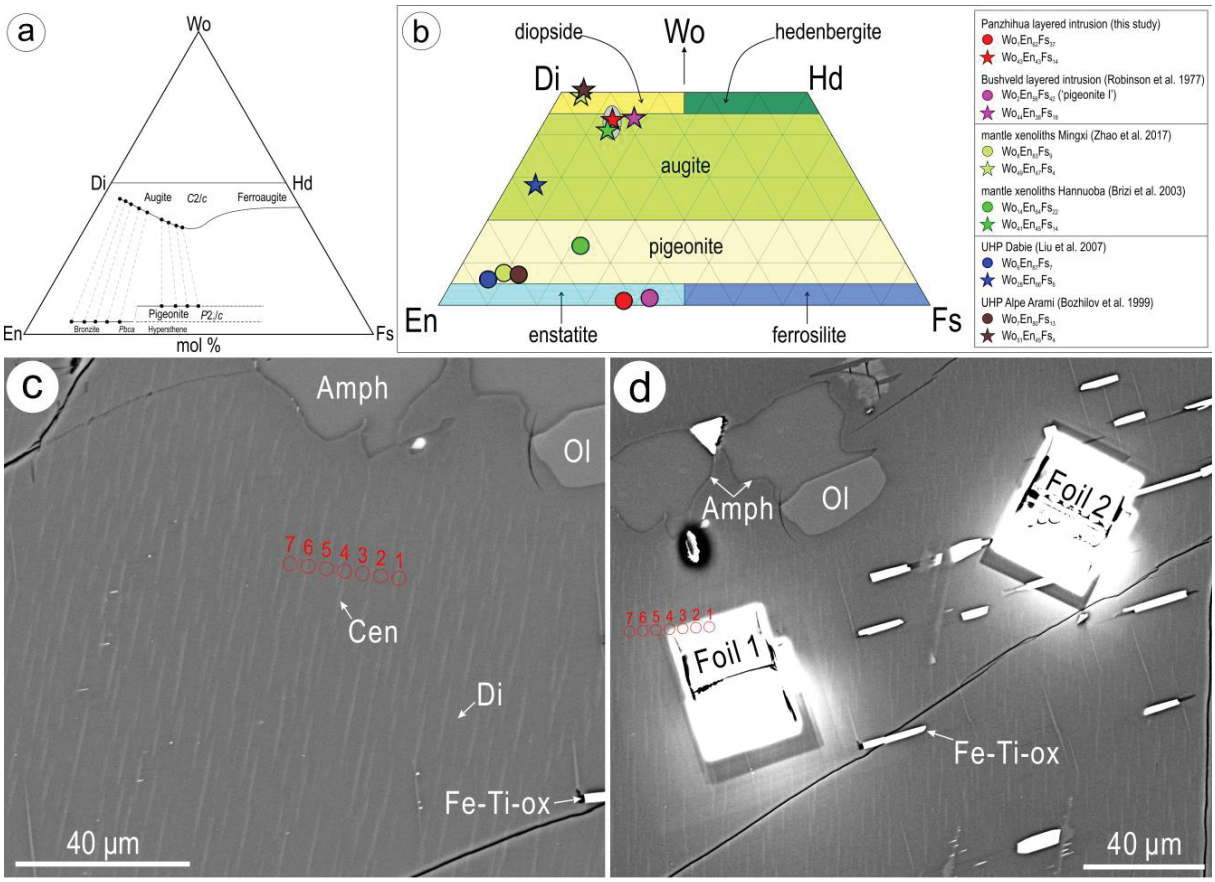

WG Pyroxene TEM manuscript Figure 1

This is a preprint, the final version is subject to change, of the American Mineralogist (MSA)
Cite as Authors (Year) Title. American Mineralogist, in press.
DOI: https://doi.org/10.2138/am-2019-6764

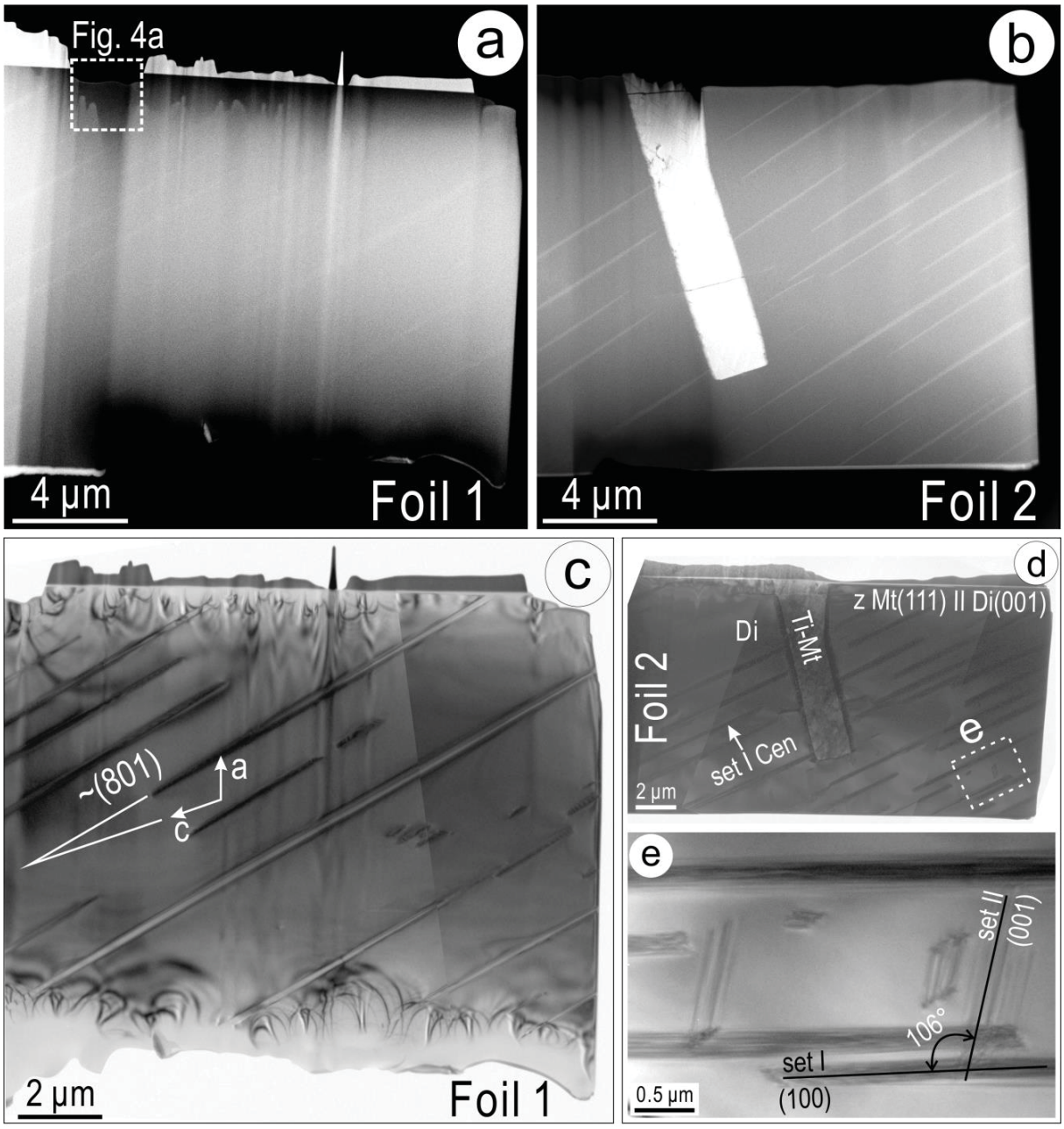

WG Pyroxene TEM manuscript Figure 2

This is a preprint, the final version is subject to change, of the American Mineralogist (MSA)
Cite as Authors (Year) Title. American Mineralogist, in press.
DOI: https://doi.org/10.2138/am-2019-6764

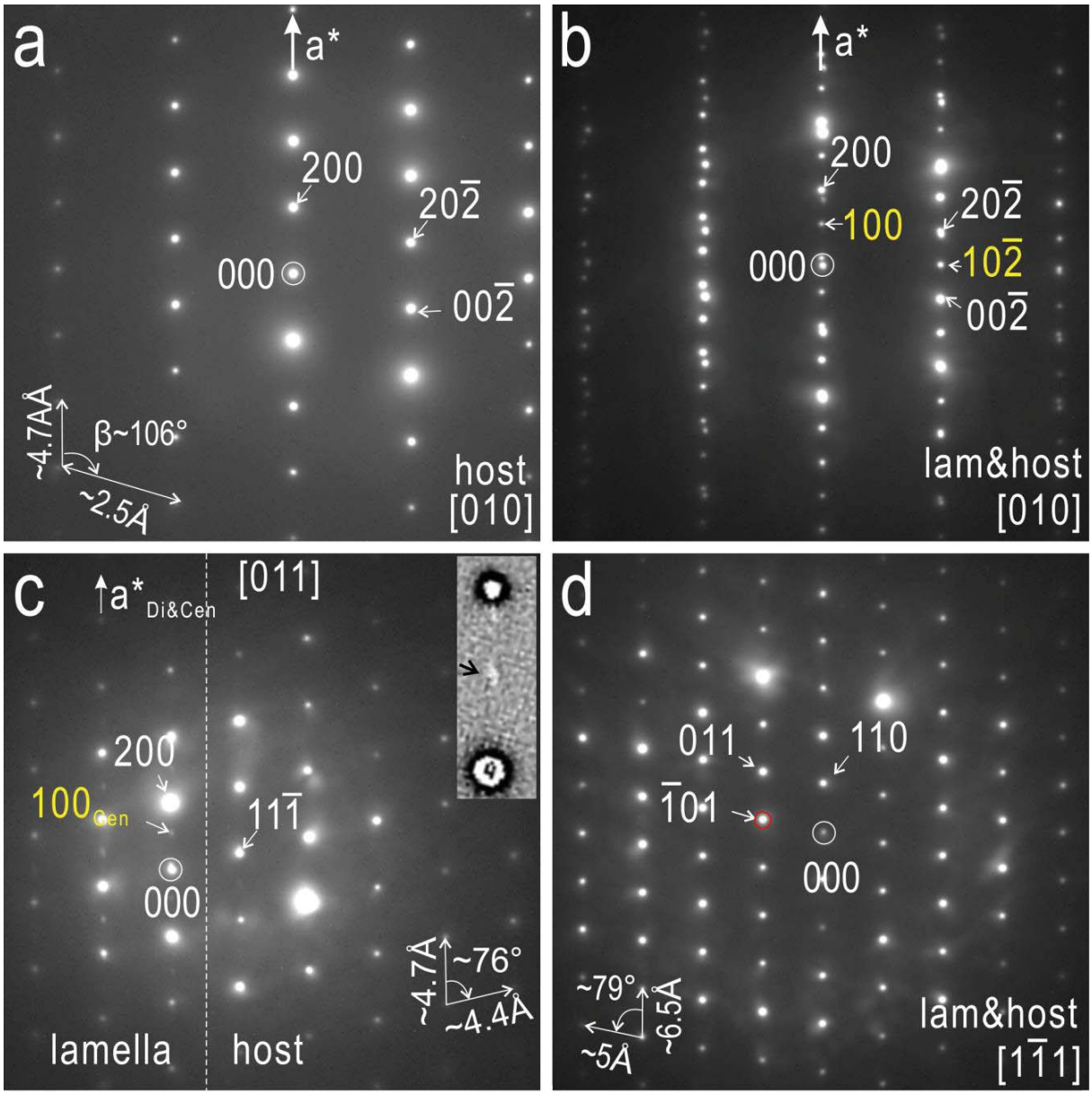

WG Pyroxene TEM manuscript Figure 3

This is a preprint, the final version is subject to change, of the American Mineralogist (MSA)
Cite as Authors (Year) Title. American Mineralogist, in press.
DOI: https://doi.org/10.2138/am-2019-6764

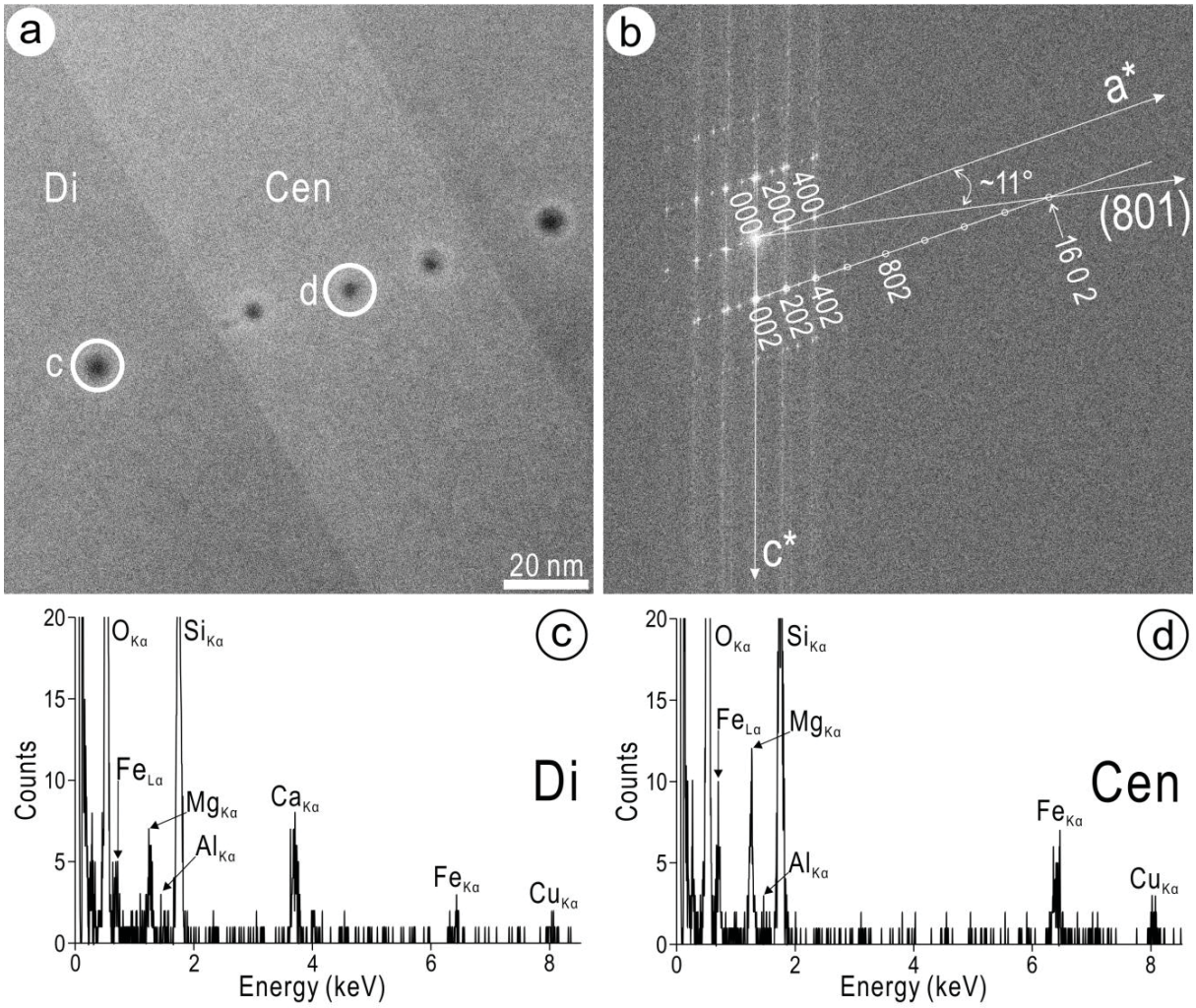

WG Pyroxene TEM manuscript Figure 4

This is a preprint, the final version is subject to change, of the American Mineralogist (MSA)
Cite as Authors (Year) Title. American Mineralogist, in press.
DOI: https://doi.org/10.2138/am-2019-6764

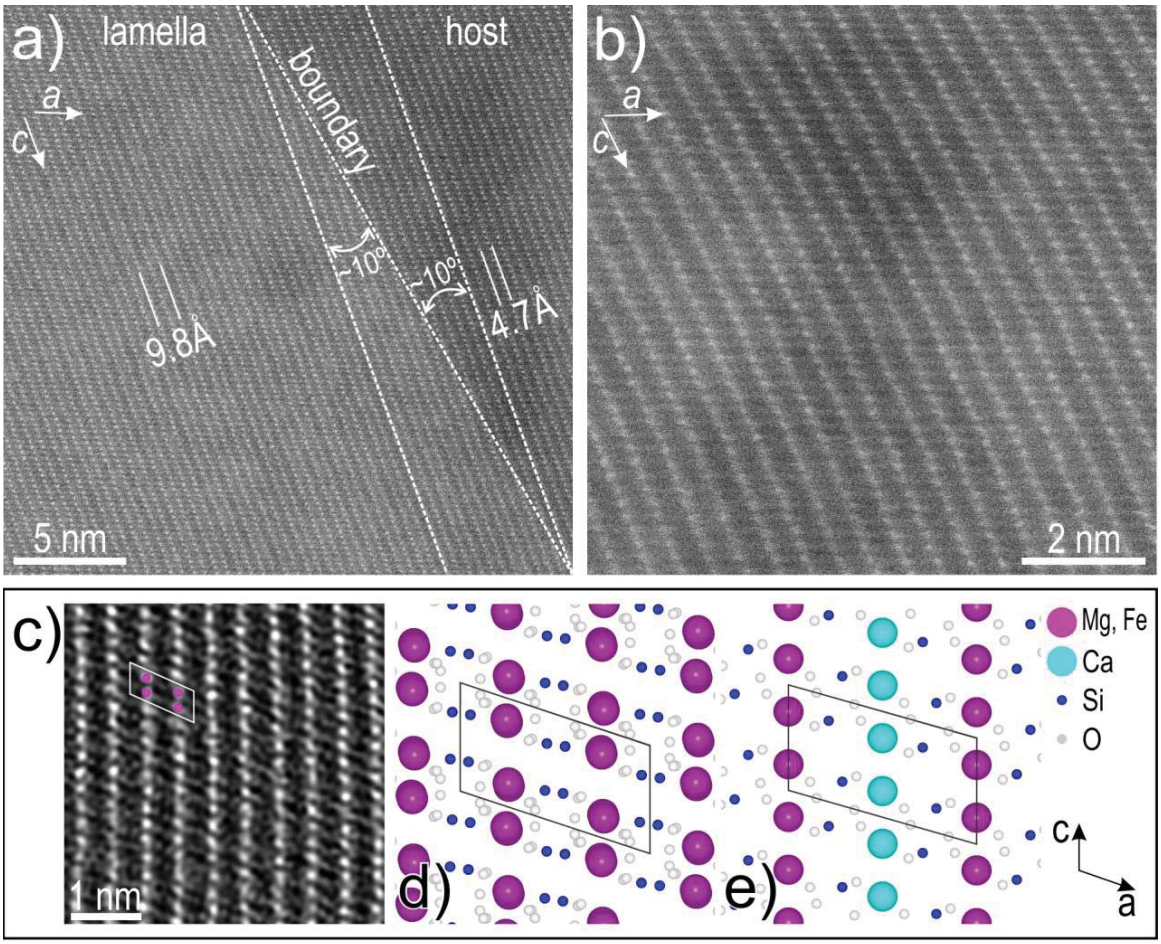

WG Pyroxene TEM manuscript Figure 5

This is a preprint, the final version is subject to change, of the American Mineralogist (MSA)
Cite as Authors (Year) Title. American Mineralogist, in press.
DOI: https://doi.org/10.2138/am-2019-6764

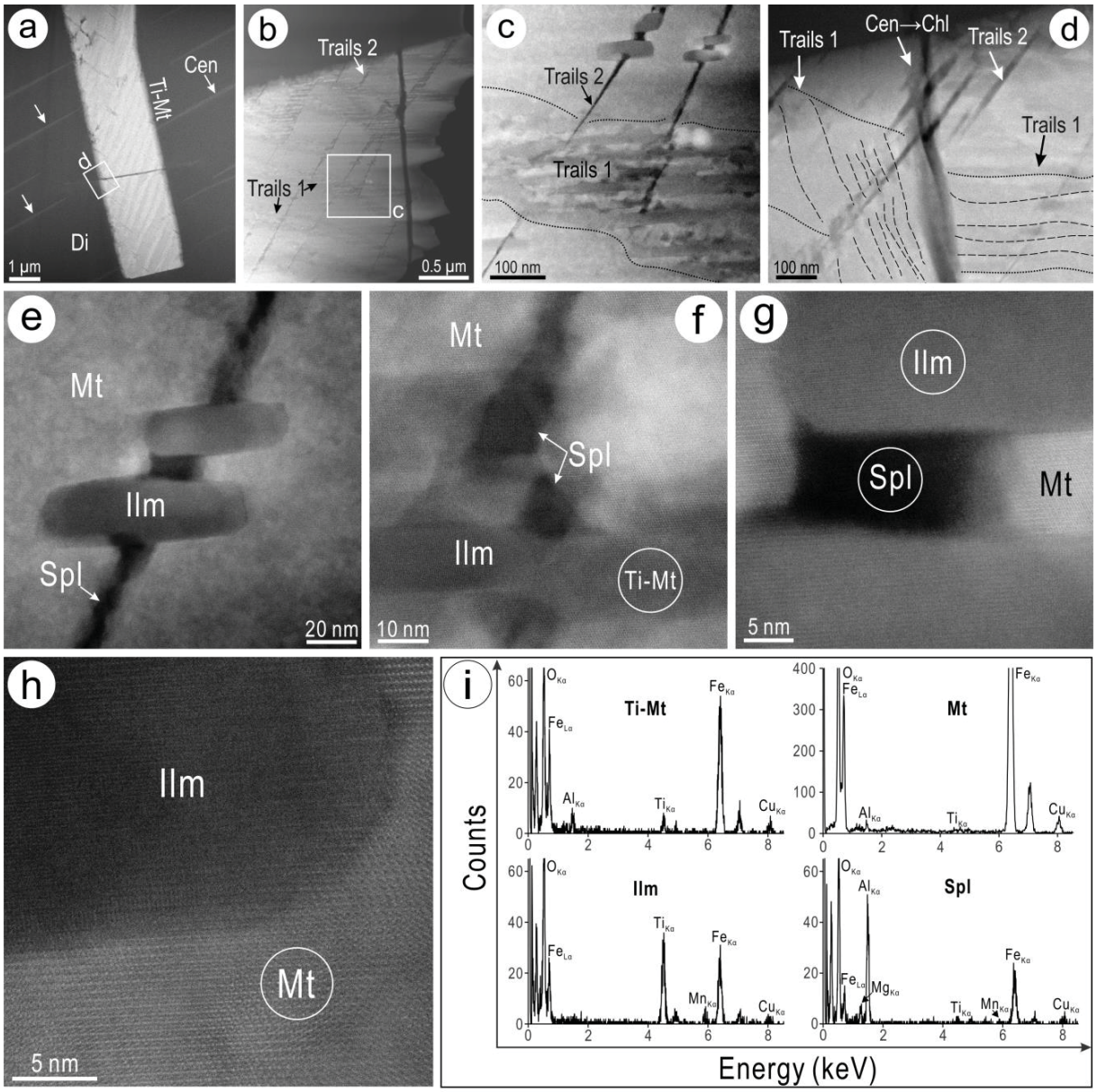

WG Pyroxene TEM manuscript Figure 6

This is a preprint, the final version is subject to change, of the American Mineralogist (MSA)
Cite as Authors (Year) Title. American Mineralogist, in press.
DOI: https://doi.org/10.2138/am-2019-6764

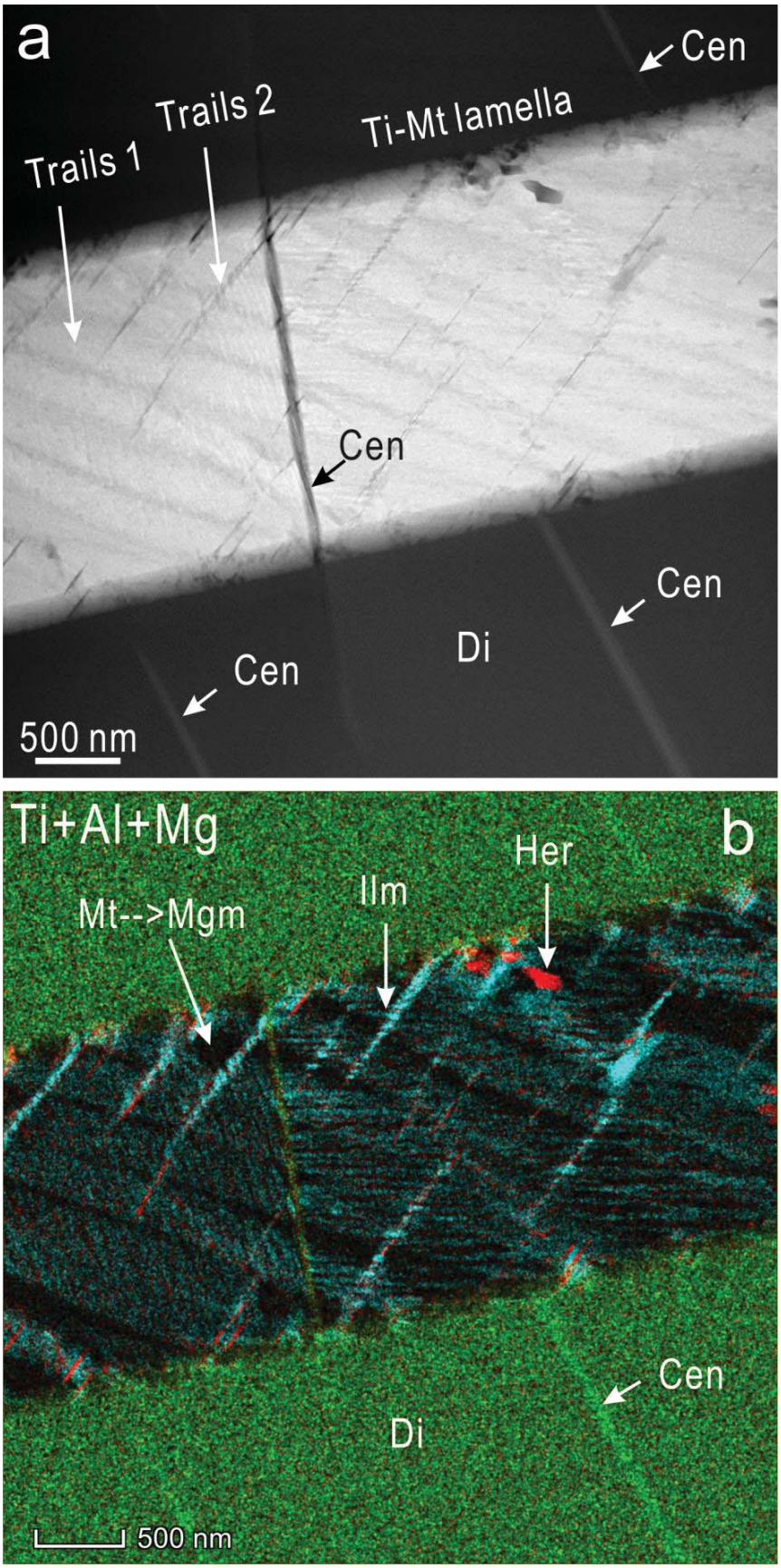

WG Pyroxene TEM manuscript Figure 7

This is a preprint, the final version is subject to change, of the American Mineralogist (MSA)
Cite as Authors (Year) Title. American Mineralogist, in press.
DOI: https://doi.org/10.2138/am-2019-6764

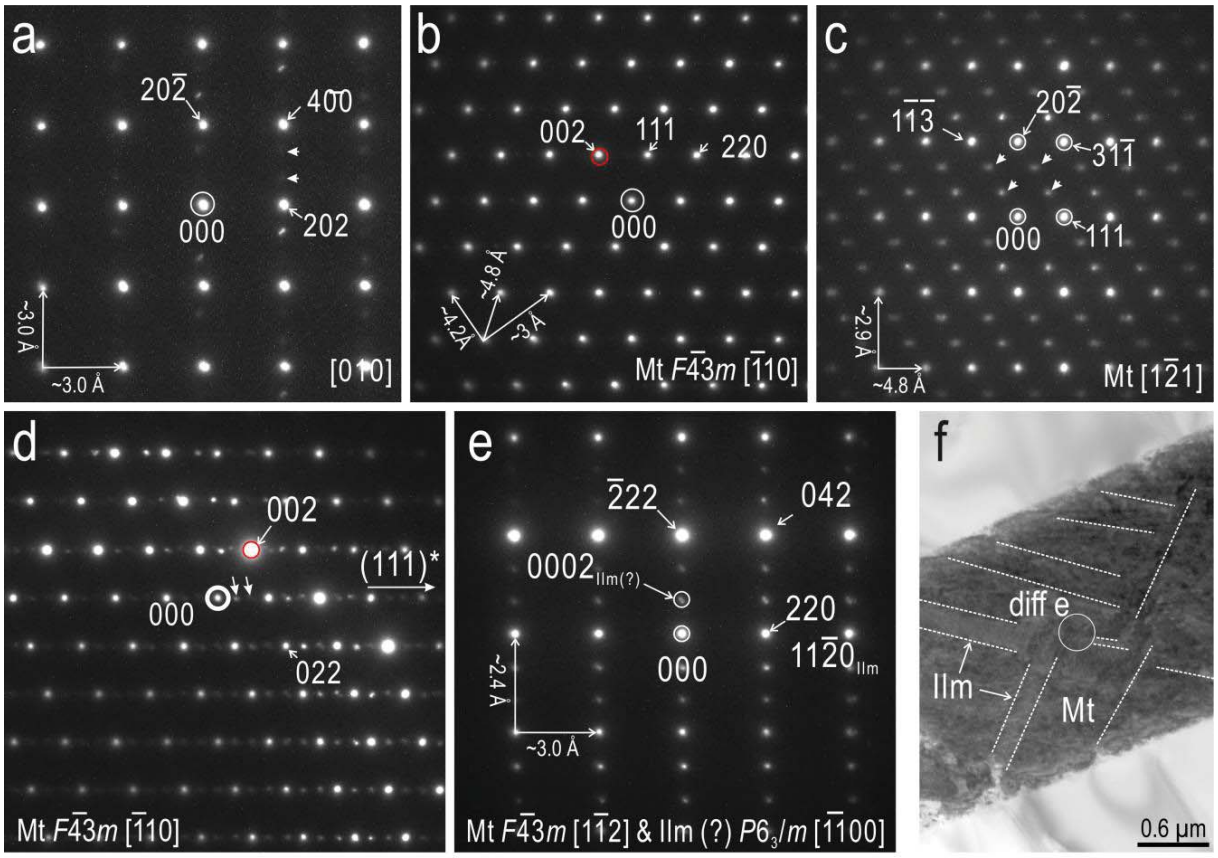

WG Pyroxene TEM manuscript Figure 8

This is a preprint, the final version is subject to change, of the American Mineralogist (MSA)
Cite as Authors (Year) Title. American Mineralogist, in press.
DOI: https://doi.org/10.2138/am-2019-6764

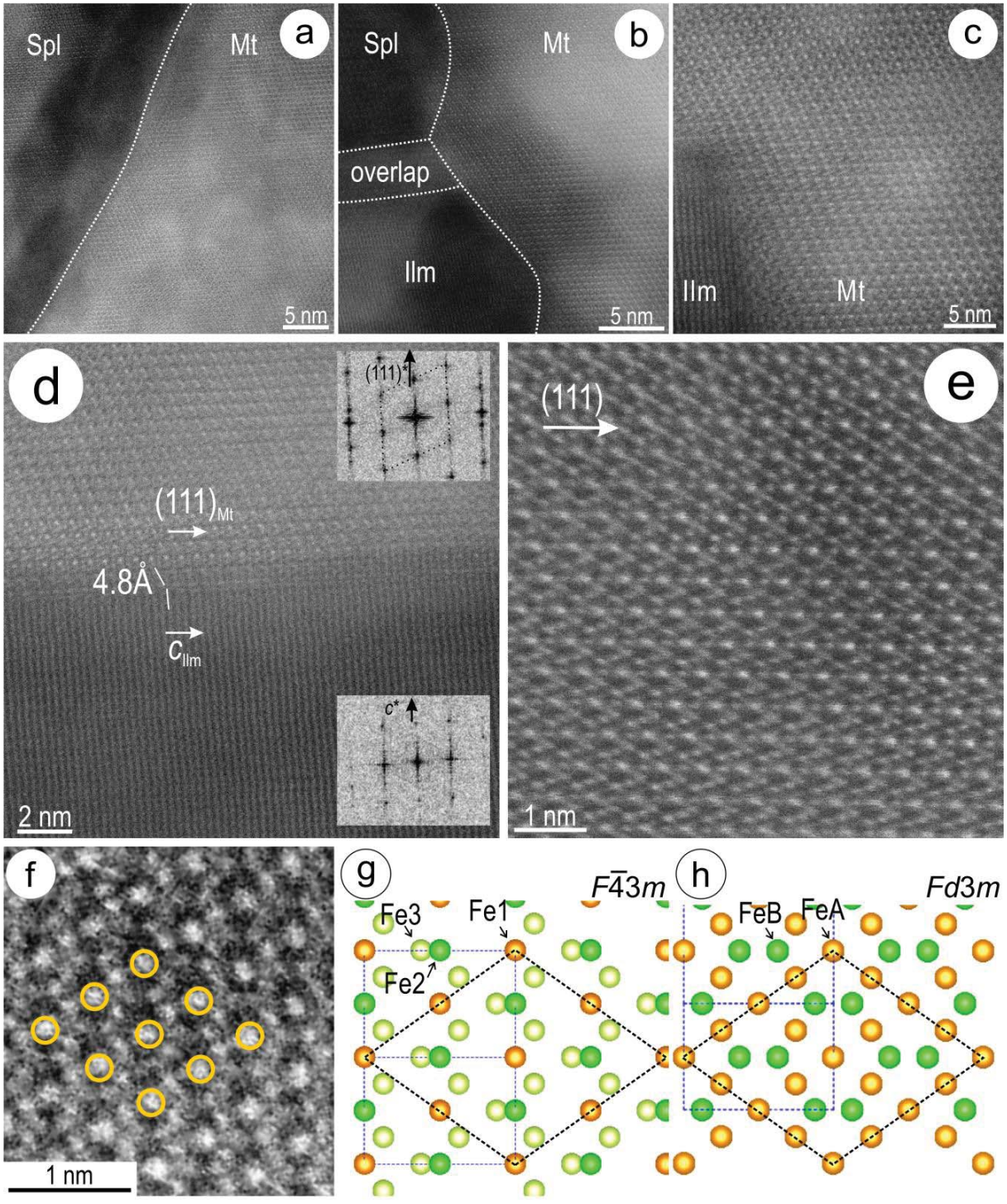

WG Pyroxene TEM manuscript Figure 9

This is a preprint, the final version is subject to change, of the American Mineralogist (MSA)
Cite as Authors (Year) Title. American Mineralogist, in press.
DOI: https://doi.org/10.2138/am-2019-6764

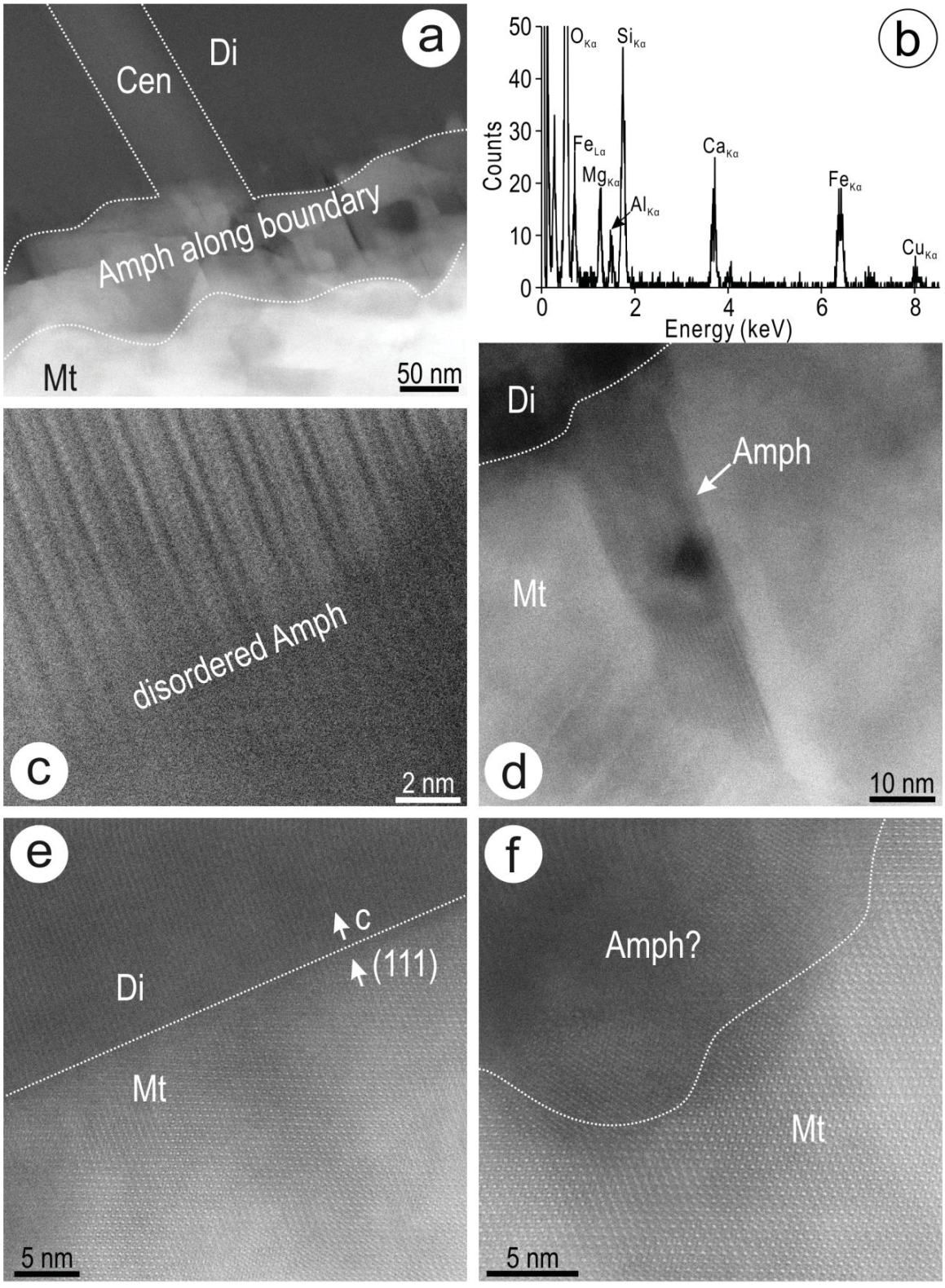

WG Pyroxene TEM manuscript Figure 10

This is a preprint, the final version is subject to change, of the American Mineralogist (MSA)
Cite as Authors (Year) Title. American Mineralogist, in press.
DOI: https://doi.org/10.2138/am-2019-6764

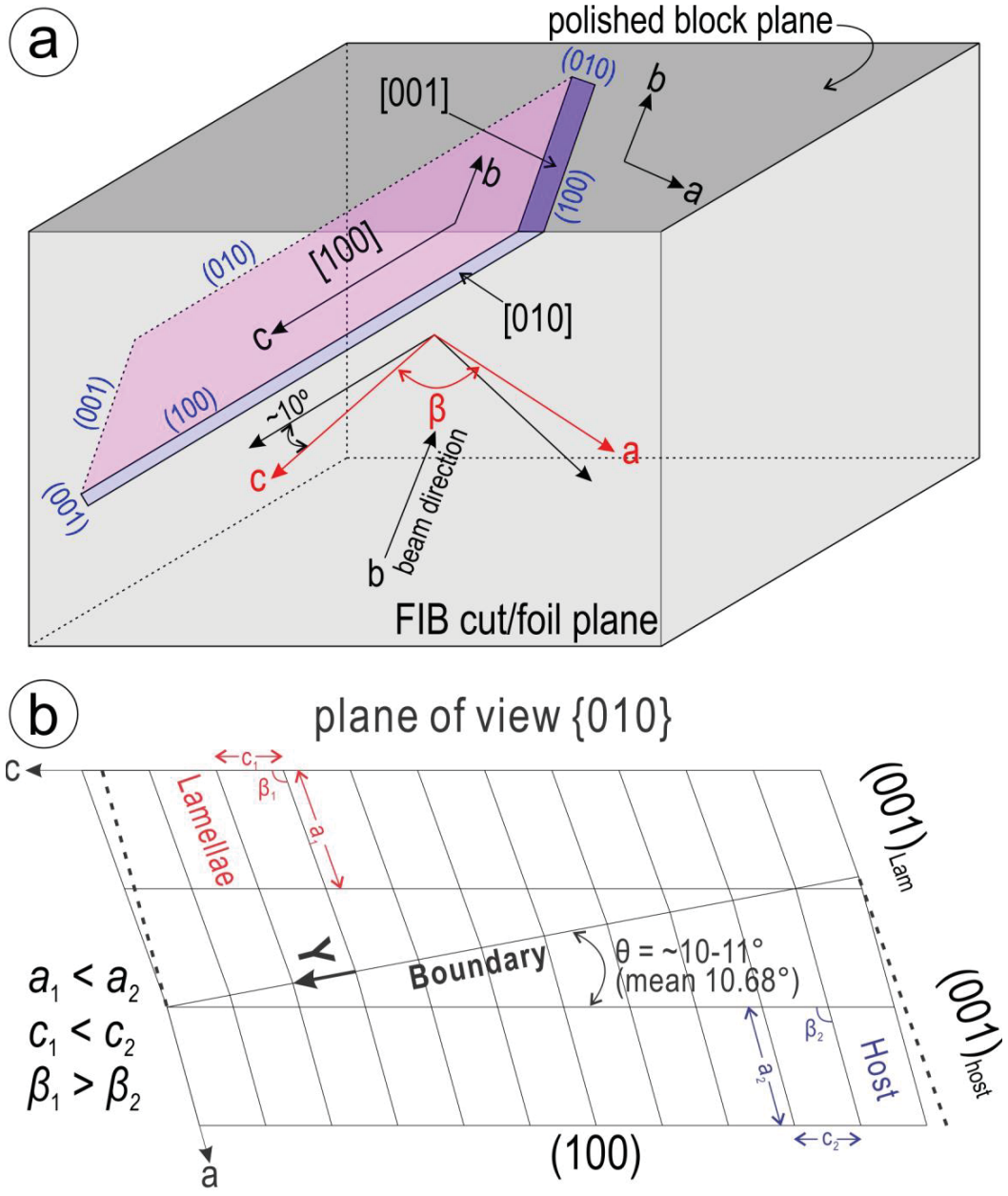

WG Pyroxene TEM manuscript Figure 11

This is a preprint, the final version is subject to change, of the American Mineralogist (MSA)
Cite as Authors (Year) Title. American Mineralogist, in press.
DOI: https://doi.org/10.2138/am-2019-6764

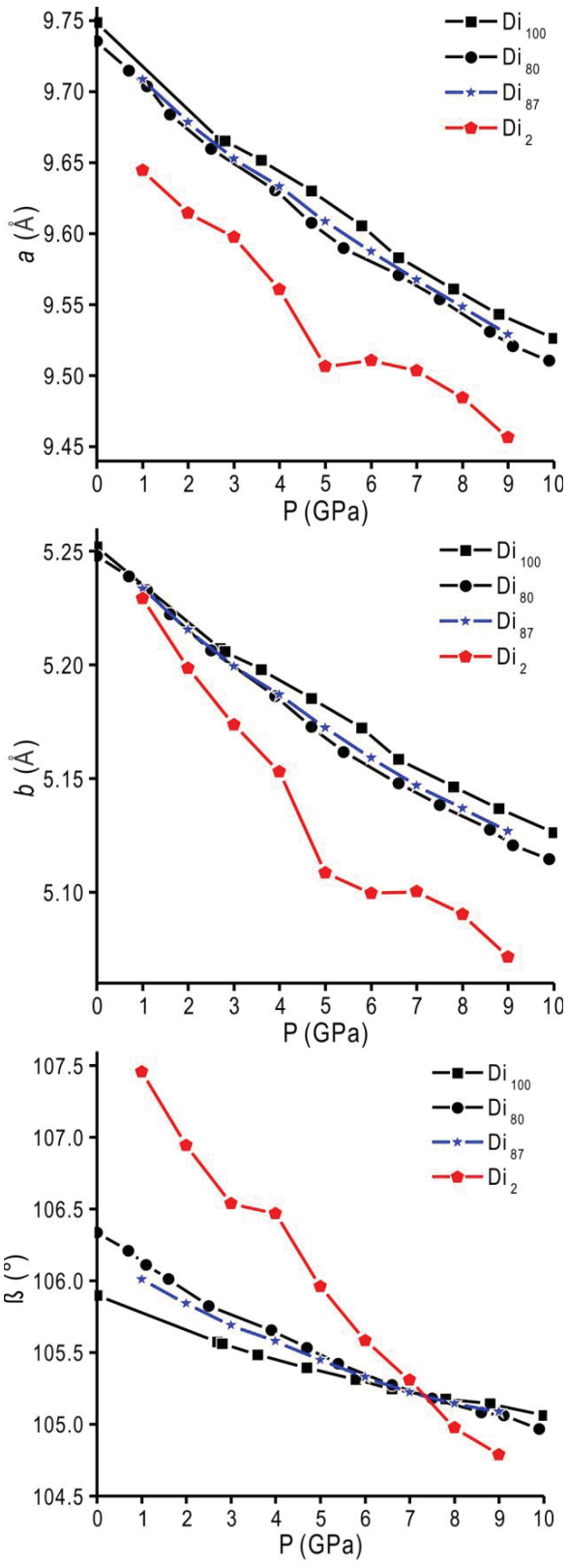

WG Pyroxene TEM manuscript Figure 12

This is a preprint, the final version is subject to change, of the American Mineralogist (MSA)
Cite as Authors (Year) Title. American Mineralogist, in press.
DOI: https://doi.org/10.2138/am-2019-6764

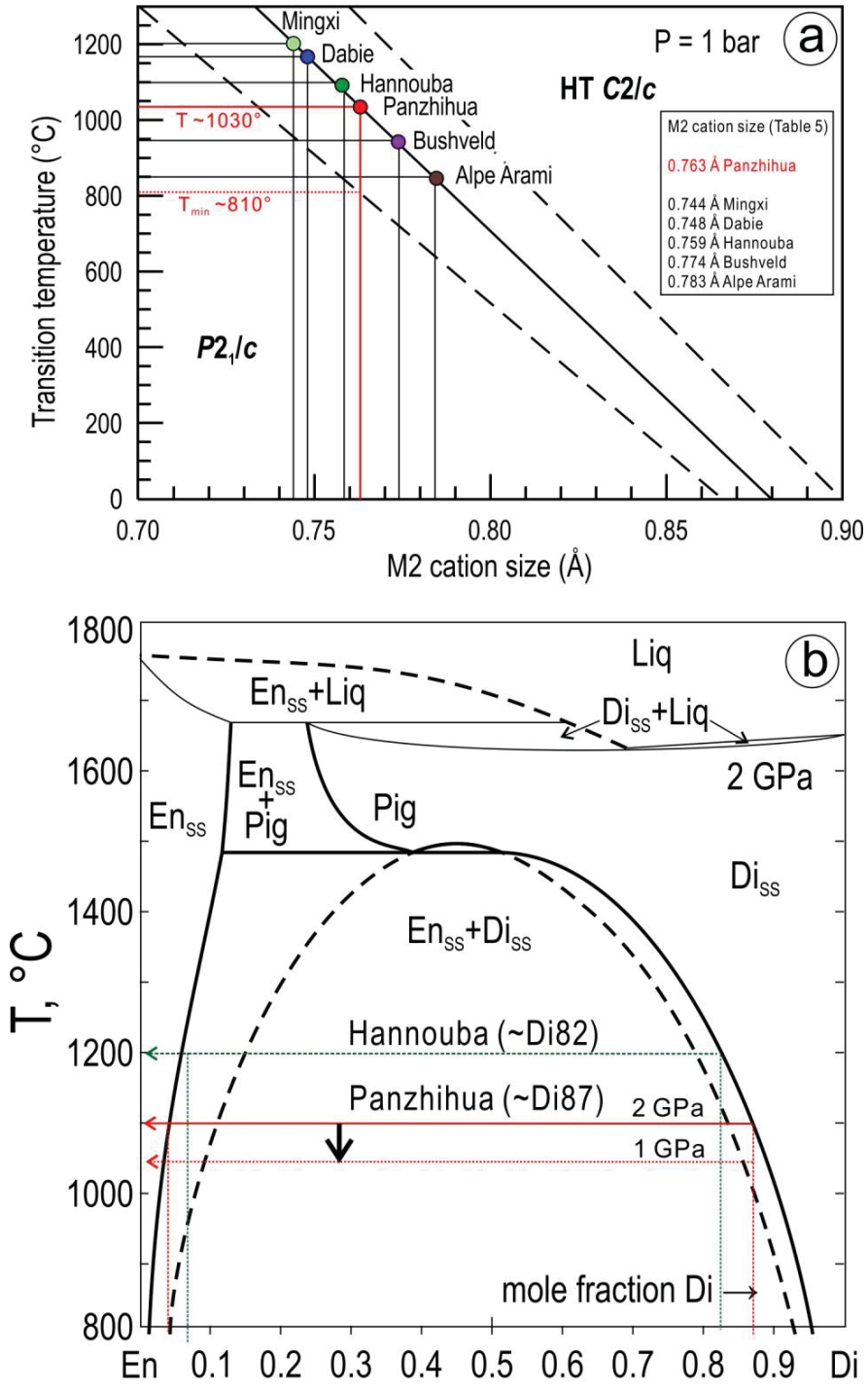

WG Pyroxene TEM manuscript Figure 13

This is a preprint, the final version is subject to change, of the American Mineralogist (MSA)
Cite as Authors (Year) Title. American Mineralogist, in press.
DOI: https://doi.org/10.2138/am-2019-6764

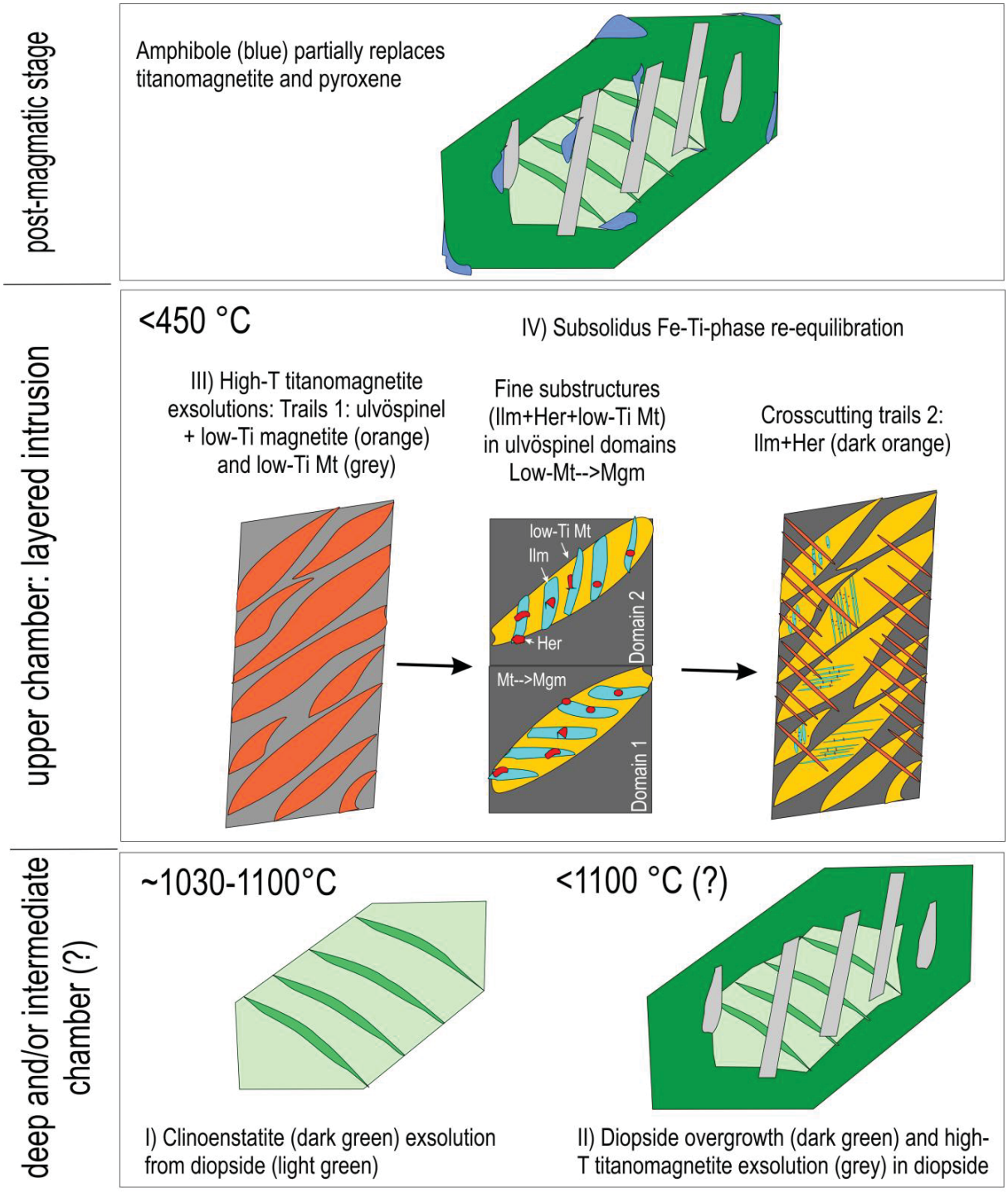

WG Pyroxene Figure 14

This is a preprint, the final version is subject to change, of the American Mineralogist (MSA)
Cite as Authors (Year) Title. American Mineralogist, in press.
DOI: https://doi.org/10.2138/am-2019-6764

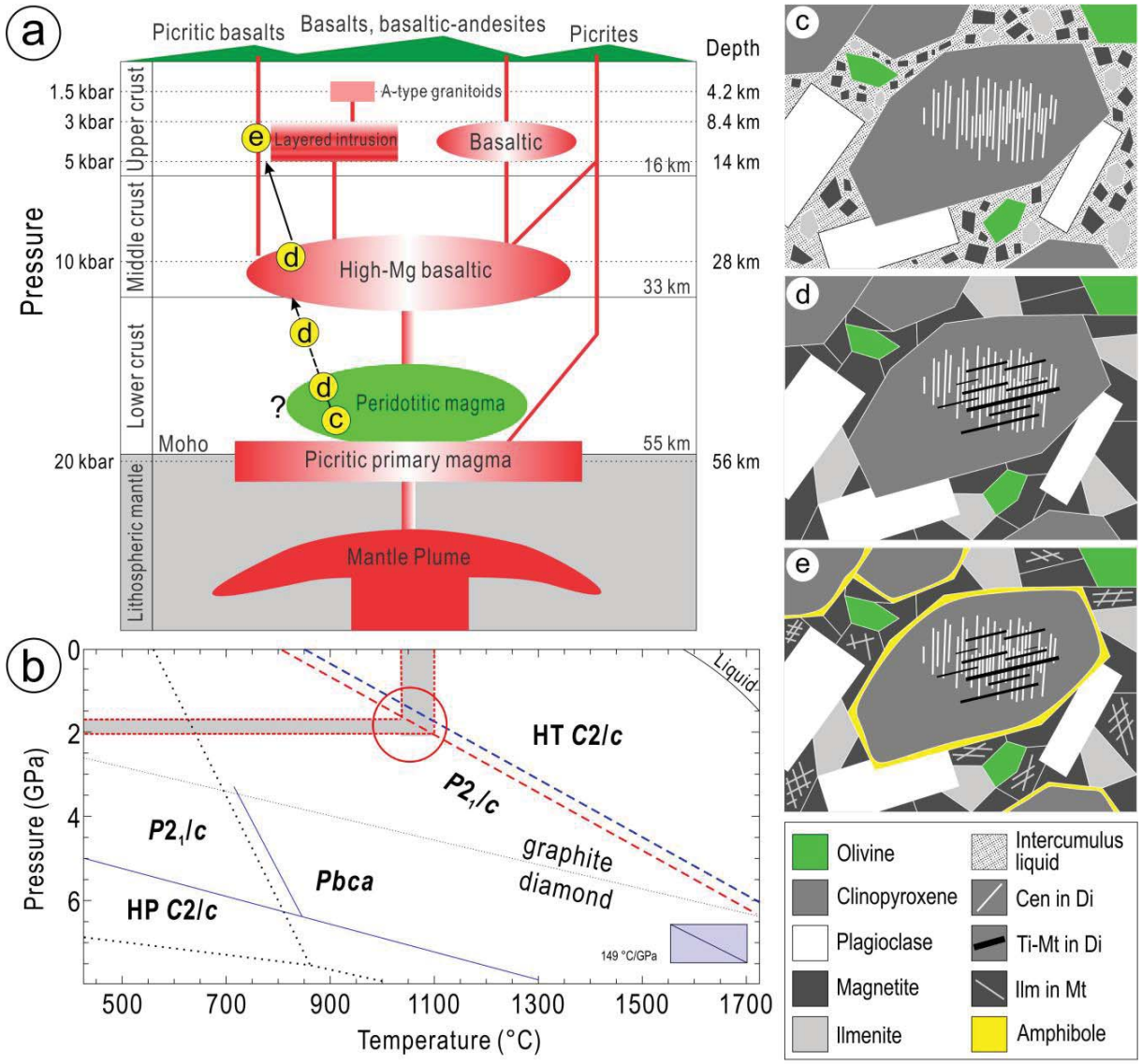

WG Pyroxene TEM manuscript Figure 15